Engineering Journal

Fourth Quarter 2024 | Volume 61, No. 4

Smarter. Stronger. Steel.

Engineering Journal

American Institute of Steel Construction

Dedicated to the development and improvement of steel construction, through the interchange of ideas, experiences, and data.

Engineering Journal (ISSN 0013-8029) is published quarterly. Published by the American Institute of Steel Construction at 130 E Randolph Street, Suite 2000, Chicago, IL 60601.

Steel Structures to Withstand the Elements: What Structural Engineers Need to Know about Corrosion

Jennifer McConnell

ABSTRACT

While regimented design processes for load-induced effects in structures are ubiquitous, similar design processes for considering corrosion resistance are lacking. This is a critical gap in the structural engineering profession as material degradation is the most common cause of diminishing structural condition for bridges and other infrastructure exposed to the elements. This results in both safety and financial consequences. This paper addresses this gap by reviewing basic principles governing corrosion, how these corrosion principles translate to real-world environments, commonly available corrosion protection systems, long-term field data assessing corrosion in varied quantified environments and associated conclusions, and practical design and maintenance strategies for improving corrosion resistance. These concepts are connected through a proposed framework for considering corrosion as a limit state that can be applied to all structures. Detailed consideration of uncoated weathering steel (UWS) bridges is provided as a pilot material and structure type for considering corrosion as a limit state. Thoughtful application of these concepts can be used to optimize corrosion resistance, improving life-cycle costs and service lives of civil engineering structures.

Keywords: corrosion, corrosions resistance, uncoated weathering steel.

CORROSION AS A LIMIT STATE

Corrosion affects nearly every industry sector. In fact, the National Association of Corrosion Engineers (NACE) estimated (in 2016) the worldwide economic impact of corrosion to be $2.5 trillion annually, equating to 3.4% of the global gross domestic product. Furthermore, the most widespread problem affecting our national transportation infrastructure is material degradation. This fact is supported by examining the causal factors for diminishing conditions of highway bridges. So, increased understanding of corrosion is a timely need to enable more widespread implementation of design and maintenance choices that lead to more durable structures.

While presently, corrosion is typically considered in the design and maintenance of highway bridges, these considerations are generally qualitative. The most current national guidance on this topic is contained in the American Association of State Highway and Transportation Officials' (AASHTO) *Guide Specification for Service Life Design of Highway Bridges* (2020). This reference highlights that, with respect to corrosion, "there is no universal solution." For example, selections between alternative corrosion protection systems are typically limited to relative comparisons between cost and qualitative performance of different options. Another example of present reliance on qualitative processes is the descriptions of different environments that are frequently applied to make choices regarding situations in which some corrosion protection systems should or should not be used. In some cases, such qualitative considerations are the best available information. However, this paper will review recent progress to enable corrosion resistance to be approached from a more quantitative—and, therefore, engineered—approach.

Furthermore, it is proposed to develop an engineered approach that takes the form of considering corrosion as a limit state. This proposed framework is analogous to the limit state equations routinely used in structural engineering, where mathematical equations require the strength of various member types to be greater than the force effects of the loads that are applied to those members. Numerous mathematical equations have been rigorously developed over decades to ensure that such strength requirements are consistently satisfied with a uniform level of safety, generally having a format similar to Equation 1:

$$\phi R_n > \sum \gamma_i Q_i \quad (1)$$

where ϕ is a resistance (safety) factor; R_n is the member resistance for a specific force effect and/or member type; and $\Sigma\gamma_i Q_i$ is the summation of the factored load effects from the governing load combination considering dead load,

Jennifer McConnel, PhD, Bentley Systems Career Development Professor and Director of the Center of Innovative Bridge Engineering, University of Delaware, Newark, Del. Email: righman@udel.edu

Paper No. 2023-16

live load, wind load, etc. It is within reason as a long-term goal to think about corrosion as a similar concept, with the corrosion resistance of our materials being designed to be greater than the corrosive effect of the environment in which they are located. For example, Equation 2 shows an equation analogous to Equation 1:

$$\phi R_c > \sum \gamma_i C_i \tag{2}$$

where ϕR_c could represent the corrosion resistance of a given material or corrosion protection system and $\Sigma\gamma_i C_i$ could represent the combined corrosion effect of environmental factors causing corrosion, such as average annual snowfall, atmospheric chloride concentrations, etc. The following sections review recent findings that can serve to develop a foundation for such equations and engineered approaches.

CORROSION AND CORROSION RESISTANCE OF STEEL

Corrosion Fundamentals

To progress the consideration of the corrosion resistance of structures from qualitative to quantitative approaches, a basic understanding of the fundamental chemical processes governing steel corrosion is necessary. Steel corrosion involves the transformation of iron (Fe) into what is typically referred to as "rust." Equations 3 through 6 illustrate one of the simpler of a few possible ways of forming rust. Equation 3 shows that the first reaction in the steel corrosion process is the dissolution of electrons from iron. This dissolution occurs quite readily when iron is exposed to any of the multiple sources of naturally occurring moisture (e.g., humidity, rain, snow) due to the natural oxidation state of iron being +2 (as in the example shown in Figure 1) or +3. Furthermore, the transformation to rust cannot proceed without moisture (H_2O) to produce hydroxide ions in the subsequent step (Equation 4) in the series of reactions leading to the formation of rust. Therefore, the presence of water is a critical factor affecting corrosion rates and thus an important factor in designing for corrosion resistance. More complicated means of forming rust similarly rely on the presence of H_2O.

$$\mathrm{Fe} \xrightarrow[\text{dissolution}]{(\textit{moisture})} \mathrm{Fe}^{2+} + 2\mathrm{e}^- \tag{3}$$

$$2\mathrm{e}^- + \tfrac{1}{2}\mathrm{O}_2 + \mathrm{H}_2\mathrm{O} \rightarrow 2\mathrm{OH}^- \tag{4}$$

$$\mathrm{Fe}^{2+} + 2\mathrm{OH}^- \rightarrow \mathrm{Fe(OH)}_2 \tag{5}$$

$$\mathrm{Fe(OH)}_2 \xrightarrow{\text{dehydration}} \mathrm{Fe}_2\mathrm{O}_3\mathrm{H}_2\mathrm{O} \tag{6}$$

Another element of concern is chlorine. Chloride ions (Cl^-) can be suspended as fine particulates in the air above bodies of salt water, which the wind can then drive onto structures in marine environments. Other sources of Cl^- are deicing agents applied to roadways for winter roadway maintenance. From a chemistry perspective, Cl^- is problematic because it serves as an electrolyte. Equation 3 shows that the first reaction for forming rust is an electrochemical reaction, with electrons traveling through films of moisture on the surface of the steel. Chlorides form dissolved electrolytes in this solution, which act as a catalyst, thereby increasing the rate at which rust forms. These facts regarding the effect of H_2O and Cl^- highlight that, while "the elements" is often thought of as a general phrase referring to weather, considering "the elements" as the chemical elements involved in quantitatively described corrosion processes provides a scientific foundation for designing for corrosion as a limit state.

Influence of the Environment on Corrosion

The discussion in the previous section explains why corrosion rates depend on the environment in which structures are located, as the presence of H_2O and Cl^- vary dramatically between locations. These variations occur due to regional variations in climate, site-specific features within a given region, and differences in exposure to water and chlorides within a given structure. These variations can be considered relative to the existing framework of macro- and micro-environments. In this framework, all structures can be classified into at least one macro-environment. For example, one version of these classifications involves four categories: coastal environments, where the concern is exposure to chlorides; industrial environments, where the concern was previously exposure to sulfur dioxide, but this concern has been mitigated by modern Clean Air regulations now in place for decades; urban environments, where the concern was previously exposure to elevated pollutants in general, which is also a negligible modern concern; and lastly, rural environments that have been and continue to be defined as being relatively benign environments. Thus, of these four macro-environment categories, only the coastal macro-environment presents a modern-day corrosion concern as it is the only one with elevated H_2O and/or Cl^-. Quantification of this category is discussed subsequently.

Micro-environments may exacerbate the corrosivity of the macro-environment due to the specifics of the bridge site, particularly due to the amount of H_2O and Cl^- at the site relative to the typical characteristics of the surrounding macro-environment. Examples of this include highway overpasses that cross over roadways treated with deicing agents for winter roadway maintenance. These bridges are exposed to higher amounts of chloride than other bridges in the same general location because road spray from the under passing roadway is transferred to the superstructure. Similarly, bridges that cross over waterways can experience

localized increases in humidity. Alternatively, vegetation in such close proximity to the structure that it shelters the structure from sunlight for the majority of the day may also increase the local humidity. And lastly, as a final example, within the coastal macro-environment, the chloride effect is highly variable due to regional variations in atmospheric chloride concentrations, which are illustrated in Figure 1. More detailed consideration of these effects for the specific example of UWS bridges is given below.

Nano-environments are a third category of environment, proposed herein, to refer to differences in exposure to water and chlorides within a given structure. For example, details like leaking joints and discontinuous deck materials allow only some portions of the superstructure to be exposed to greater than normal amounts of H_2O and possibly the Cl^- dissolved in this water. Similarly, details that trap debris or provide inadequate drainage allow water and debris to collect on isolated areas of the structure, creating a continuously wet environment. While these effects are sometimes considered as part of the micro-environment, it is useful to distinguish between this classification of nano-environments compared to the definition of micro-environments given previously because owners, designers, and maintenance engineers have different levels of control over these two categories of environments. There is generally little to no control about the general site (i.e., micro-environment as defined herein) for a bridge. On the other hand, engineers and owners have full control of the nano-environment of the structure. Suggestions on best practices for exerting this control to achieve more corrosion resistant structures are described subsequently.

Corrosion Protection Systems

Corrosion protection systems for steel can be organized in three categories. These three categories apply to structural steel used in bridges and the exposed elements of buildings and include numerous types of paint that are typically formulated to be used in specific combinations to form multilayer paint systems. These are often termed "liquid applied coatings." Other coating types are categorized as "thermal applied coatings," with the most common examples of this being galvanizing and metallizing. In both of these coating systems, molten zinc or a blend of zinc and aluminum is used to provide corrosion protection. The third category is "uncoated steels," in which case the corrosion resistance is provided by additional alloying elements within the steel. There are two general types of uncoated steels presently specified for typical use in the United States. One type is known as weathering steel [or, when used uncoated

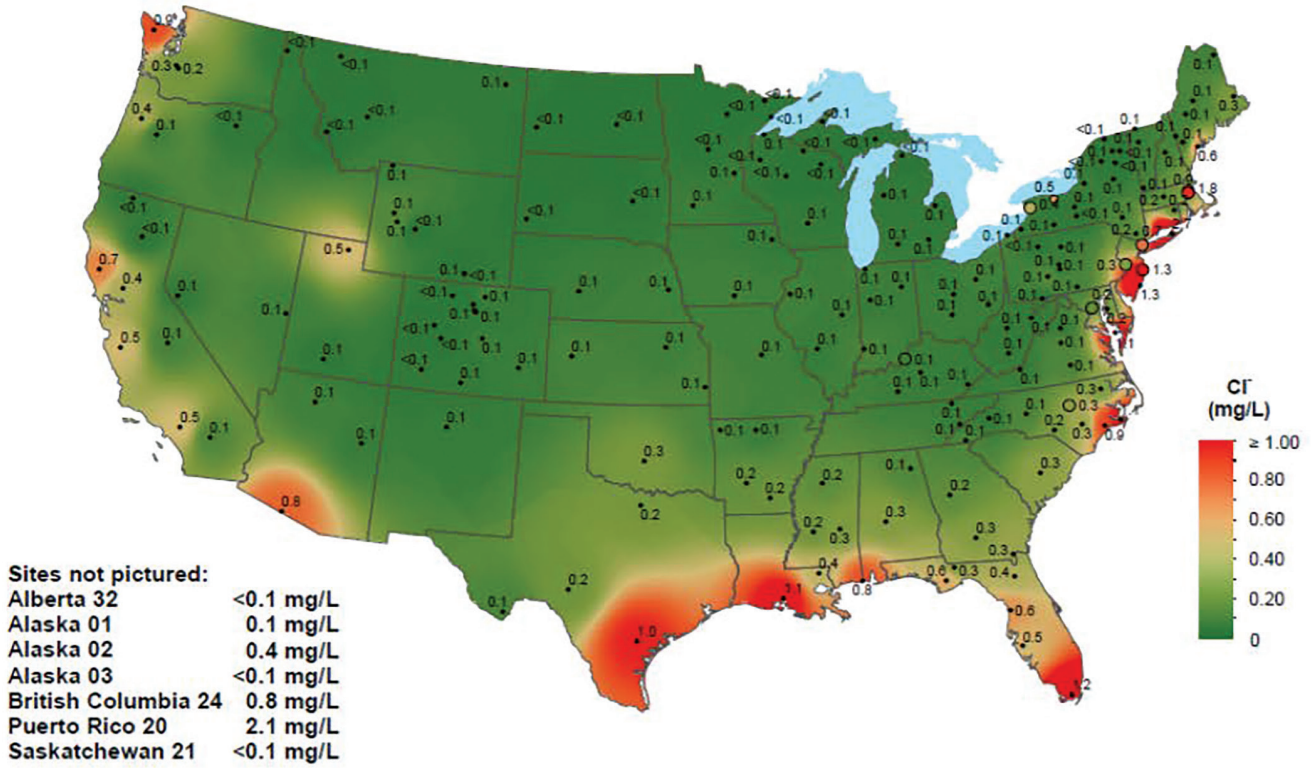

Fig. 1. Chloride concentrations in the continental United States (NADP, 2020).

as intended, uncoated weathering steel (UWS)], and there are specifications for several grades of UWS [e.g., via ASTM A588 (2019) for buildings and ASTM A709 (2021); AASHTO M 270 (2021) for bridges]. The other type of uncoated steel presently available is designated as 50CR (previously designated as ASTM A1010), due to the fact that corrosion resistance is provided by a relatively high percentage of chromium (Cr) (ASTM, 2021; AASHTO, 2021). Additional information on each of these types of corrosion protection systems is well summarized by Kogler (2015), who provides an overview of the scientific principles governing corrosion protection as well as practical considerations for each of these corrosion protection systems.

These various corrosion protection systems have differing performance in different environments as well as different costs, making it difficult to optimize the selection of the corrosion protection system. While additional quantitative and objective information on both performance and cost is needed, recent work has started to provide quantitative comparative data. First considering performance, an aggregate view of comparative field performance was compiled by McConnell et al. (2022) as quantified by the superstructure condition rating (SCR) [Federal Highway Administration (FHWA), 1995] based on data from eight state departments of transportation that identified UWS, galvanized, metalized, and painted bridges within their agency. While the SCR takes several factors into consideration (such as for steel bridges, fatigue cracks and other visual signs of overstressed members, damage resulting from vehicular impacts, missing bolts in structural connections), corrosion is the most common cause of decreasing SCR. Thus, when reviewing these ratings for an extensive sample size, prior work has supported that SCR give a general indication of steel bridge durability (McConnell et al., 2024) despite their qualitative and subjective nature. Therefore, the SCR for the bridges identified by these departments of transportation was downloaded from the National Bridge Inventory (FHWA, 2022) and analyzed.

Figure 2 shows linear regression lines of the SCR versus age of each corrosion protection system considered (which were found to be a reasonable compromise between simplicity and accuracy compared to higher order curve fits). One notable observation from Figure 2 is that the slopes of the performance of the galvanized, UWS, and painted bridges are remarkably similar. Furthermore, Figure 2 shows that the relative performance of these three corrosion protection systems is such that galvanized bridges generally have the highest SCR ratings, painted bridges have the lowest SCR ratings, and UWS bridges have performance (as quantified by SCR) in between these two types. The metalized bridges in this dataset initially have the highest SCR, but the trend for this dataset deteriorates more quickly than the other corrosion protection systems. However, it should be noted that the sample size of the metalized bridges was very small, representing less than 1% of the dataset, and that older metalized bridges may not be representative of modern methods. Additional analysis of this data can be found in McConnell et al. (2022). The results in Figure 2 inform general trends but do not definitively determine the performance of a certain corrosion protection system at a given age or, more critically, a given environment given the significant effects of the environment on durability. Therefore, this data can be supplemented with the data compiled by Kogler (2015), who proposed deterioration rates and expected lives of different corrosion protection system options in environments where such data is available.

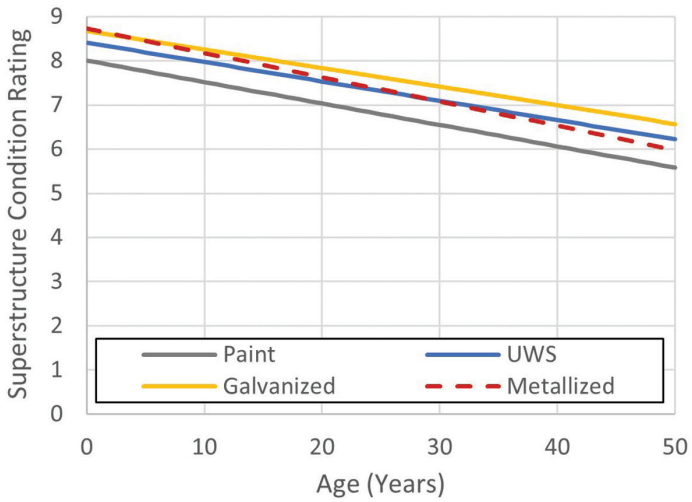

Fig. 2. Linear regression lines of condition versus age for various corrosion protection systems (not for extrapolation).

The ideal framework for choosing between alternative corrosion protection systems would be to compare such considerations of performance with the corresponding life-cycle cost, which accounts for both the first cost and maintenance costs over the lifetime of a structure. For example, materials with higher first cost are generally coupled with lower maintenance costs. However, sufficient data on longevity—and the multitude of factors that influence longevity—is not presently available to execute such an analysis. Yet, one aspect of cost for which there is presently relatively comprehensive high-quality data is the first cost of the most common corrosion protection systems. These have been quantified by a 2020 fabricator survey performed by the American Institute of Steel Construction (AISC), the results of which are summarized by Figure 3. This data indicates that the two UWS options [UWS with painted ends, which is recommended best practice for UWS (FHWA, 1989)], and UWS with painted ends and fascia (which is a preferred practice of some owners for aesthetic reasons) were consistently the lowest cost. The third lowest cost option is a single coat of inorganic zinc (IOZ) paint. It is noteworthy that even the maximum cost of these three minimum cost choices is lower than the minimum cost of the seven remaining choices. The two UWS options also have minimal maintenance requirements. Therefore, in situations where these three corrosion protection systems can provide adequate corrosion resistance, they are preferred options because they will also result in minimizing life-cycle cost. For this reason, the following section summarizes research related to specific analysis of the environments in which UWS provides adequate corrosion resistance.

QUANTIFIED ENVIRONMENTAL EFFECTS FOR UWS BRIDGES

Introduction

Prior to the start of the research summarized herein, an existing resource for quantifying the corrosivity effects of different environments was the International Standards Organization (ISO) Standard 9223 (2012), which can be applied to any structure type (e.g., buildings, bridges, and other infrastructure types). This standard categorizes the corrosivity of all environments into six categories, labeled C1 to C5 in terms of increasing severity and with the sixth, most severe, category labeled as CX. The classifications into these categories are a function of the average temperature, average relative humidity, and average annual chloride and sulfur dioxide deposition rates, which are mathematically related to the corrosion rates for carbon steel, zinc, copper, and aluminum.

Figure 4 shows the classification of locations in the continental United States and portions of Mexico and Canada into these ISO categories. From Figure 4, it is observed that the majority of the continental United States is in category C2 (low corrosivity), most of the remainder is in category C3 (medium corrosivity), relatively small areas are in category C4 (high corrosivity), and no areas are in any of the remaining categories (very low, very high, or extreme corrosivity). In other words, the ISO 9223 classifications are relatively coarse, such that the observed performance of UWS bridges (and perhaps other corrosion protection systems) does not correlate well to these classifications. This is not particularly surprising considering that UWS is not a material type explicitly considered in this specification.

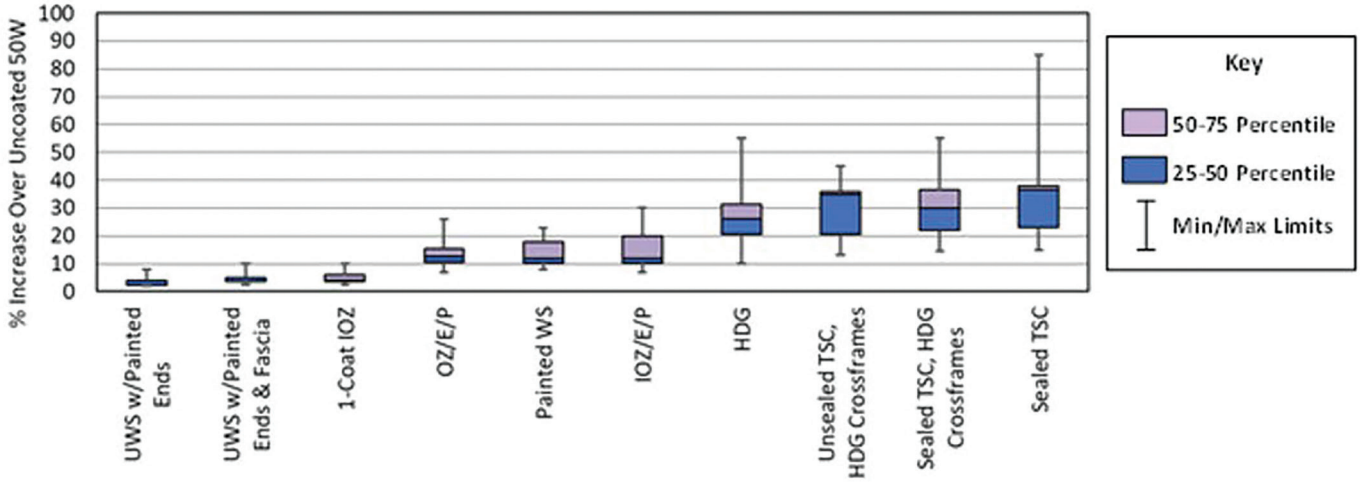

Fig. 3. Box and whisker plot of relative first costs of common corrosion protection systems (AISC, 2022).

Furthermore, this classification system lacks the ability to consider the influences of the micro-environment, which has been shown to be of significant importance. Therefore, while this classification system has general usefulness for describing the corrosivity of an environment, the results below advance this concept by being specific to UWS and considering micro-environment effects.

Methodology

The quantifications of environments that are discussed subsequently are based on three types of data: field data for 34 bridges that was collected as part of research specifically focused on the performance of UWS; in-depth review of owners' reporting of UWS condition (as quantified by element-level condition state data reported in accordance with AASHTO 2001, 2011, or 2019 procedures) for 200 bridges; and superstructure condition ratings of 10,000 UWS bridges in 48 states, the District of Columbia, and Puerto Rico. These three data types have different amounts of refinement to the data and, consequently, the number of bridges evaluated by those methods. This results in a dataset that is well balanced in terms of the depth of the data analysis as well as its breadth, allowing comprehensive conclusions to be developed.

A key aspect of the field work and review of owners' reporting on UWS condition was based on methodical selection of the bridges to be evaluated. The organizational structure for these selections was based on forming groups of bridges in geographic proximity to one another, which were termed "bridge clusters," that targeted the macro- and micro-environments of greatest interest. Specifically, the two environments that were clearly of most widespread concern based on an owner survey (McConnell et al., 2024) were highway overpasses over roadways treated with deicing agents and bridges in coastal environments. The intersection of these two effects for bridges along the northern coastlines was also evaluated. As summarized by Table 1, two condition-related categories were examined in each of these environments: "inferior" and "good" performing. These categories captured the most extreme performance situations by sampling the worst-performing bridges as well as not only good-performing bridges, but bridges that were performing well despite being located in a harsh environment at an advanced age. Table 1 shows the states representing these environments and conditions in the field work and review of owners' reporting. The geographic range of each cluster was generally within a 50-mi radius, which typically resulted in all of the bridges for a given cluster being located within a single state, but included bridges in two states in some situations, as shown in Table 1.

Within each cluster, the bridges were systematically selected for review of owners' reporting based on statistical analysis of key parameters influencing corrosion (e.g., site-specific humidity, distance to the coast, etc.). A subset of these were selected for field work based on capturing the range of performance within a cluster. By structuring the bridge selections in this way, a full range of the effects of many of the most severe macro-environments in the United States can be evaluated, and by including multiple bridges within each cluster (10 to 28 based on the number of influential parameters and the diversity of the environments within the clusters), the effects of different micro-environments within these macro-environments were also quantified. Full details on the cluster bridge selections and associated data can be found in McConnell et al. (2024).

Sample Field Data

One data type resulting from the field evaluations was ultrasonic thickness measurements, which is the metric that is most readily correlated with structural performance. Field

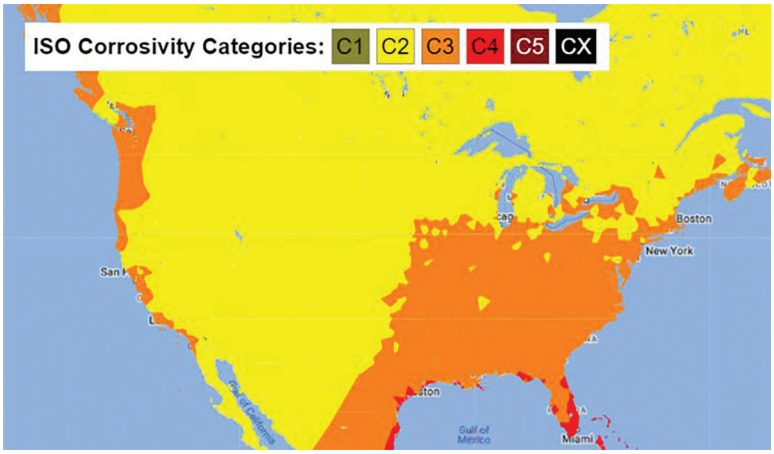

Fig. 4. International Standards Organization corrosivity categories for locations in continental United States (NIBS, 2023).

Table 1. Overview of Cluster Categories and Locations			
	Environment		
Condition	Deicing	Coastal	Deicing + Coastal
Inferior	MD/VA	LA/MS	CT
	MN	NC	—
	IA	—	—
Good	NY	TX	NH
	CO	NC	—
	OH	—	—

measurements of plate thicknesses obtained from a handheld ultrasonic thickness meter (after minor surface preparation) can be compared to the nominal thickness of the corresponding plate indicated on the structural plans. This comparison can be used to provide an estimate of thickness loss. While this is considered a minimum estimate because the original actual thickness may have exceeded the nominal specified thickness due to plate rolling tolerances, these estimates can be used to update structural capacity calculations (e.g., for load-rating purposes) if significant losses are found that warrant such an evaluation.

Figure 5 shows the estimated thickness losses based on measurements from two locations indicative of representative performance (i.e., away from improperly designed or maintained areas) on each of 21 bridges relative to the corresponding age of the structure. This data is plotted relative to the upper bounds of section loss (represented by solid lines) that are expected to occur in the ISO environmental corrosivity categories discussed previously [based on an earlier ISO draft (1988) reported by Albrecht et al. (1989)]. In particular, the upper bound to the "high" corrosivity category is of interest because discussions with stakeholders (as part of the research summarized herein) reached a consensus that this is a reasonable threshold for the upper limit of corrosion that is considered acceptable. This decision was made in part because extrapolating this threshold line results in less than 1/16 in. of thickness loss after a 75-yr service life, which is viewed as a reasonable compromise between economy and safety relative to plate rolling and inspection tolerances.

Comparing the field data shown in Figure 5 to the high corrosivity category threshold, approximately half of the data points fall above this threshold. In other words, approximately half of the dataset exhibited worse performance than desirable, suggesting that the environment in which these bridges are located should be identified and

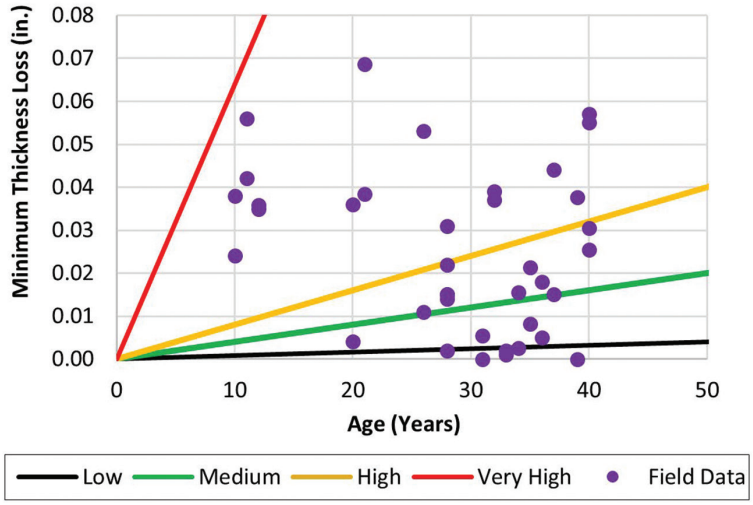

Fig. 5. Section loss of bottom flanges versus age of bridge for UWS field bridges, plotted relative to corrosivity categories.

that designs in these environments need more consideration. This data is a key finding supporting the recommendations contained in the following subsection.

Another data type resulting from the field evaluations was soluble chloride concentrations absorbed within UWS samples. This was measured by scraping the outer layer of corrosion by-products from representative locations of the girders (as described with respect to the Figure 5 data), collecting this material, then performing laboratory analysis of it using ion chromatography. This data can be thought of as representing a primary cause of corrosion because it is measuring chloride concentrations, a key factor in the corrosion process. Figure 6 shows this data for two representative subsets of bridges—those in coastal environments and those serving as highway overpasses in environments where deicing agents are used. This shows that the chloride concentrations caused by road spray containing dissolved deicing agents (from underpassing roadways) reaching the superstructure can be significantly higher than the chloride concentrations experienced by bridges in coastal environments. In fact, on average, the chloride concentrations for the bridges serving as overpasses to roadways treated with deicing agents was 10 times higher than the corresponding chloride concentrations on coastal bridges that were not in regions where deicing agents are regularly used. This data is another key finding supporting the recommendations contained in the following subsection.

Results

The overall objective of the field work described earlier was to establish quantifications for environments where UWS does not perform satisfactorily. The quantifications of the combinations of parameters that create such severe conditions for the two general environments where this occurs that were of greatest concern to bridge owners—coastal environments and overpasses over roadways treated with deicing agents—are summarized later. In addition, quantifications are also provided for high time of wetness environments, which was an environment of concern qualitatively described in prior work (FHWA, 1989). These quantifications of environments presume reasonable design, detailing, and maintenance practices in accordance with FHWA's (1989) long-standing guidance on UWS and should, therefore, be considered as a supplement to these recommendations. The practical translation of this approach is that these results are not a means to avoid poor performance associated with known problematic details, such as leaking joints and details that trap moisture. Rather, these guidelines focus on the "overall performance" of bridges, which is a term meant to represent performance independent of the effects of poor detailing or maintenance, as these issues are better addressed through appropriate design and maintenance practices, as discussed in the next section. Fuller details on the analysis of these environments can be found in McConnell et al. (2024).

Coastal Environment

Table 2 provides the quantitative definition of coastal environments for UWS. This definition is a combination of a distance to the coast less than 1 mi, a humidity score of at least 0.65 [which corresponds to average monthly relative humidity exceeding >65% for each month of the year and

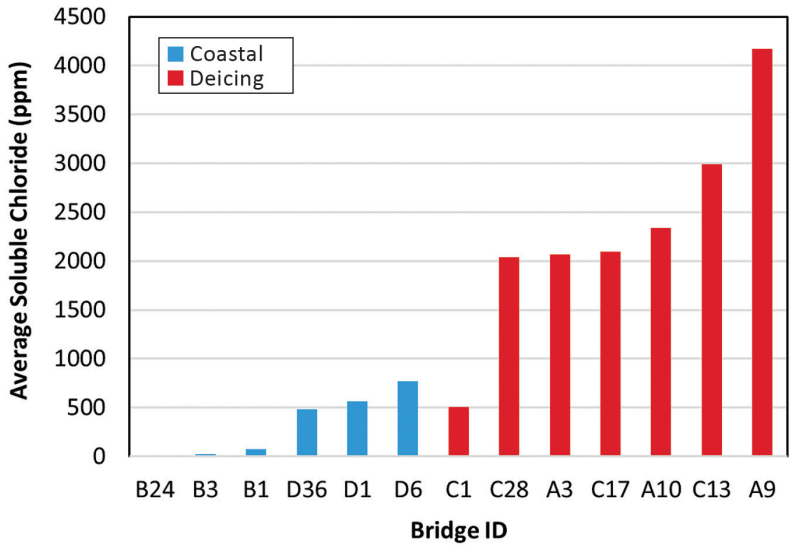

Fig. 6. Average soluble chloride concentrations for representative coastal bridges and highway overpasses in environments where deicing agents are used.

Table 2. Quantitative Definition of Coastal Environment for UWS *(Note: All four criteria must be simultaneously satisfied)*		
Parameter	**Value**	**Context**
Distance to coast	≤1 mi	Small
Humidity score	≥0.65	Average monthly relative humidity exceeding >65% for each month and >75% for at least 2 mo per year
Atmospheric Cl^-	≥0.565 ppm	90th percentile value
Crossing type	Waterway	—

>75% for at least 2 mo per year (see McConnell et al., 2024, for additional details)], and a 90th percentile value (relative to the national UWS inventory) of atmospheric chloride concentration for a bridge that also serves as a waterway crossing (due to the greater severity of this micro-environment in coastal locations). There were no observed instances of UWS bridges with unsatisfactory overall performance in coastal environments that were not waterway crossings. Figure 7 provides a map of the locations where the three quantified variables defining a coastal environment simultaneously occur. Table 2 and Figure 7 demonstrate that the coastal environment for UWS is a relatively limited geographic region. While this definition of a coastal macro-environment shares some similarities with the C4 macro-environment in Figure 4, given that they are both dependent on chloride exposure and humidity, more northern locations are included because it is not dependent upon temperature and is limited to a smaller distance to the coast since this is an explicit consideration in only the definition of a coastal environment for UWS waterway crossings.

Deicing Environment

Table 3 provides the quantitative definition of a deicing micro-environment for overpasses over roadways treated with deicing agents where UWS does not consistently perform satisfactorily, or "heavy deicing environments" for brevity. Table 3 illustrates that there are three combinations of vertical under-clearance, average daily traffic (ADT) under the bridge, average annual snowfall, and atmospheric chloride concentration that, when simultaneously satisfied, quantitatively define a heavy deicing environment. It is noted that the combination of vertical under-clearance, ADT under the structure, and average annual snowfall are proxy for quantifying the amount of chlorides from deicing agents that reach UWS superstructures (because site-specific deicing agent data is not widely available) while the atmospheric chloride concentration can further elevate chloride concentrations in marine environments. While the coastal environment was observed as being relatively limited, 11% of the current inventory of UWS bridges

Fig. 7. Continental U.S. locations meeting definition of coastal environment for UWS waterway crossings.

Table 3. Quantitative Definition of Heavy Deicing Environment for UWS *(Note: All five criteria for a given environment must be simultaneously satisfied)*			
Label	**Inferior Performance Environment 1**	**Inferior Performance Environment 2**	**Inferior Performance Environment 3**
Crossing type	Highway	Highway	Highway
Vertical under-clearance (ft)	Any	≤18	≤18
ADT under (count)	≥100,000	≥10,000	≥4,000
Average annual snowfall (in.)	≥18	≥22	≥22
Atmospheric Cl^- (ppm)	NA	NA	≥0.1

falls into one or more of the heavy deicing environments quantified by Table 3. This (combined with the data previously reviewed in Figures 5 and 6) indicates that greater caution is warranted in the use of UWS as highway overpasses in heavy deicing environments.

High Time of Wetness Environment

The third category of environments where inferior overall performance of UWS has been sometimes observed is those with frequent high rainfall, high humidity, and persistent fog. These environments can be concisely quantified by time of wetness, which is the number of hours of year where the combination of temperature and humidity allows condensation to form on metal. ISO (2012) brackets time of wetness into five ranges labeled as T1 to T5, with T5 being the highest time of wetness. Figure 8 indicates the time of wetness categories for various locations throughout the continental United States as compiled by Chase (2012). Comparing this data to the locations where inferior performance of UWS is observed that is not attributed to other factors described in previous sections, it is found that all known instances of these bridges are located in T5, which is limited to very localized areas along the coastline of the Pacific Northwest, while also having significant vegetation. Therefore, time of wetness category T5, representing greater than 5,500 hr/yr, is suggested as being a quantification for this environment of concern.

Other Environments

In addition to the three categories of environments quantitatively discussed previously, two other environments where UWS should be used with caution have been previously identified by FHWA (1989). These are industrial areas and low water crossings. However, industrial areas are a concern that has been mitigated due to Clean Air Act regulations. All known existing standards relating to UWS that quantify a threshold on sulfate (the chemical basis for the concern regarding industrial environments) either directly

Fig. 8. Time of wetness categories for continental U.S. locations (Chase, 2012).

or indirectly refer to sulfate concentrations of 250 μg/m^3 or higher. In contrast, the current maximum sulfur dioxide emissions limit by the U.S. EPA is 200 μg/m^3. For these reasons, and because UWS bridge owners in the United States have not reported any problems with UWS bridges that are attributed to proximity to industrial sites, industrial environments are suggested as being an obsolete consideration for UWS bridges.

Low-level water crossings are the only environment of concern that has been historically quantified for UWS. Decades of applying the current FHWA guidelines of cautious use of UWS within 10 ft or less of vertical clearance over stagnant, sheltered water or 8 ft or less over moving water suggest that these limits are at least adequate, and most likely conservative, for providing good-performing UWS. It is suggested that a more relevant consideration may be the propensity for flooding at the bridge site that results in the structure being submerged. More significantly, flood events also frequently lead to trapped debris—and, therefore, trapped moisture—on the superstructure. Flooding considerations have the capability to be quantified by metrics such as various intervals of flood stages (e.g., 50-yr, 100-yr) compared to the vertical clearance and the frequency of exceedance of these metrics.

APPLICATIONS FOR DESIGN AND SERVICE LIFE EXTENSION OF BRIDGES

Considering corrosion as a limit state has implications for both the design and maintenance plans of new bridge designs as well as for the maintenance practices and possible rehabilitation of existing bridges. These considerations allow new and existing bridges to achieve longer service lives. From the perspective of new bridge designs, consideration of corrosion as a limit state may be most readily incorporated into service life design procedures, relative to traditional design procedures largely focused on strength. Service life design is an evolving approach but significant progress on this has been made recently through the publication of the Federal Highway Administration's *Service Life Design Reference Guide* (Hopper et al., 2022). This guide serves as a framework for assessing relevant deterioration mechanisms and then designing corresponding elements accordingly, both through the initial design and determining timelines for anticipated future maintenance needs. As data sets for specific materials in various environments become available, such as the data described earlier, these quantifications can be used to improve the rigor of service life designs by more specifically considering corrosion as a limit state.

While it is uneconomical (and often unnecessary) to design every component or every bridge for a maximum service life, the general goal should be for the structure to be in acceptable condition when it becomes functionally obsolete. Figure 9 conceptually illustrates the goal in terms of the condition of a structure versus time for three alternative scenarios. The dotted line represents a design without careful consideration of degradation mechanisms while the dashed line shows the improvement in performance that results from designs that thoughtfully consider material degradation. Yet, the solid line illustrates that it is only through thoughtful design and maintenance that bridges are generally in acceptable condition when they become functionally obsolete. The following subsections summarize best practices on these topics.

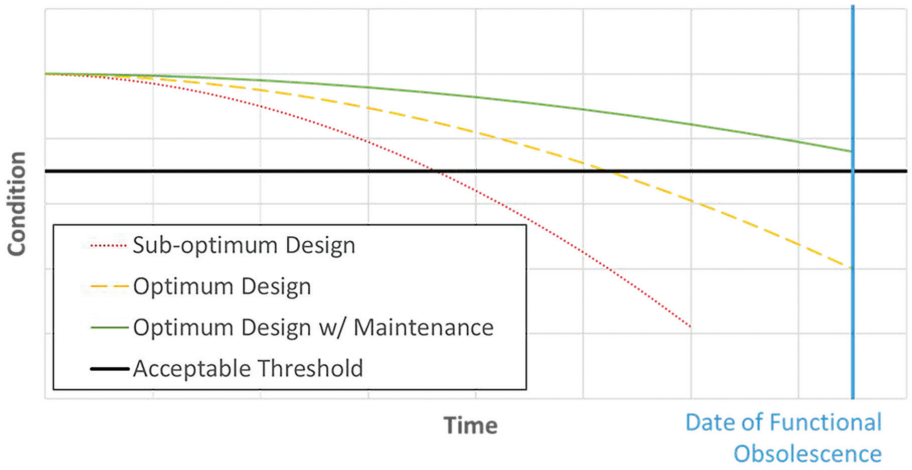

Fig. 9. Theoretical condition versus time relationship in various scenarios.

Design Considerations: Where to Design Using UWS

In considering corrosion as a limit state or when adopting service life design, choosing an appropriate corrosion protection system for the given environment is a critical design consideration. Using UWS as an example because extensive research has been done on whether UWS is an appropriate corrosion protection system for numerous environments, guidelines for the environments in which to use or not use UWS are available. Such guidelines originated with a 1989 technical advisory on the use of UWS from FHWA. Later, FHWA sponsored research to update these guidelines (McConnell et al., 2024), which was summarized in the previous section. This and other research, as well as practical experiences, were used to develop updated guidelines on the use of UWS in different environments (AISC, 2022). A conceptual representation of these guidelines is shown by Figure 10. In this flowchart, the macro-environment is first classified as being either high time of wetness, coastal, or none of the above. The definitions of high time of wetness and coastal were quantified in the previous section. Then, the micro-environment is also evaluated for its potential to increase the chloride concentration or humidity (i.e., exposure to water) relative to the macro-environment. Specific examples of this are waterway crossings in coastal environments, the quantification of a heavy deicing micro-environment that was given in the previous section, low-water crossings susceptible to submersion of the UWS members, and sites with dense vegetation that shelters even the exterior UWS members from sunlight for the majority of the day.

If both the macro-environment and the micro-environment increase the humidity or chlorides, then UWS would not be recommended; instead, a more durable corrosion protection system would be recommended. For example, a paint system could be used, either at the onset or anticipated as future need. While paints may not necessarily perform better than UWS, repainting when paint deteriorates is a relatively common and convenient practice to readily provide continued corrosion protection and an acceptable structural condition with respect to corrosion. If neither the macro-environment nor micro-environment are severe relative to the preceding definitions, then UWS would be the ideal material choice from the perspectives of least first-cost, least life-cycle cost, and proven corrosion performance.

The intermediate recommendation in Figure 10 of "use UWS thoughtfully" results when only the macro-environment or the micro-environment results in increased humidity or chlorides. In these situations, some diminished performance of UWS is likely. However, because of the severity of these environments, it cannot be assured that most other materials or corrosion protection systems would perform ideally either. Therefore, designers and owners may opt for an alternative corrosion protection system or, because of a greater understanding of the behavior of UWS resulting from the extensive long-term studies on this material, use UWS thoughtfully. One example of thoughtful use of UWS is including a sacrificial thickness as a corrosion allowance. Given the data previously shown in Figure 5, a ⅛ in. sacrificial thickness to bottom flanges is a recommended value for most situations because this envelops the expected corrosion losses and results in typical plate thicknesses. Another example of thoughtful use is creating a maintenance plan. While maintenance of all bridges

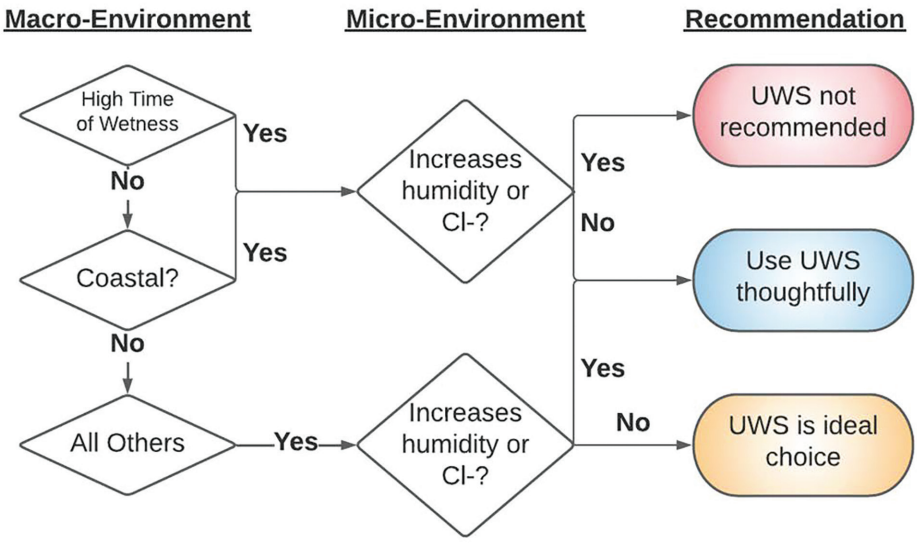

Fig. 10. General concept for UWS use based on macro- and micro-environment (AISC, 2022).

is vital, the concept of a maintenance plan is to thoughtfully plan and program for potential maintenance needs before there is an apparent problem. This minimizes deferred maintenance problems and improves bridge performance. Maintenance considerations that may be included in maintenance plans or generally considered for extending the service lives of existing bridges are further discussed in the following section. Both sacrificial thicknesses and maintenance plans are further discussed in AISC (2022).

Maintenance Considerations

Maintenance considerations can either be preprogrammed in a maintenance plan at the time of original design, implemented into a maintenance plan that is developed during the service life of a bridge, or implemented individually or in combination as the need arises. The most effective maintenance considerations for steel bridges, and possibly other bridge types, include consideration of the drainage of the runoff (that is often salt-laden in winter months) from the bridge deck and other surfaces where water may collect. The overarching concept of these considerations is preventing this runoff from reaching the structural components of the structure, through well-designed and well-maintained drainage systems. Best practices for initial design of drainage systems are readily available in FHWA (1989) and AISC (2022) guidelines. While the implementation of these design practices is widespread, maintaining these drainage systems is not. In particular, leaking bridge joints are a frequent occurrence, which leads to widespread deterioration of structural members beneath these leaking joints. Therefore, it is strongly recommended that these joints be repaired or replaced before they deteriorate or as soon as possible thereafter. Lifespans on typical joint lifespans compiled by Milner and Shenton (2014) are also summarized by AISC (2022), which can be used for maintenance planning purposes. Ideally, joint maintenance should be programmed at internals not to exceed the anticipated life span of the joint.

Alternatively, to prevent leaking joints and the associated structural deterioration, the ideal scenario is to eliminate joints wherever possible. A common means of doing this is by using integral or semi-integral abutments. Additional information on jointless bridges and the practical constraints thereof is summarized by AISC (2022). A newer strategy that achieves the same effect from a drainage standpoint without complicating the structural design is to place the expansion joint beyond the back wall with a drainpipe or trough that collects the runoff and discharges it away from the superstructure. For example, this is a widespread strategy used by the Virginia Department of Transportation, which has a standard detail for this known as a Virginia Abutment (Figure 11) and has been retrofitting numerous bridges throughout their jurisdiction with this design detail.

Another aspect of a maintenance plan or other periodic maintenance is bridge washing and cleaning. The clear benefits of these practices for UWS bridges are documented by McConnell et al. (2024), where statistical analyses revealed that for highway crossings specifically, bridge washing was the second most highly correlated variable with bridge performance (as quantified by superstructure condition ratings), second only to age of the structure. Best practices for bridge washing are outlined by AASHTO (2023) and recommended frequencies for washing various bridge components are given by AISC (2022).

Lastly, a final aspect of a maintenance plan or other periodic maintenance can include maintenance painting. This is an essential item for bridges that are initially painted. For uncoated steels used in environments where thoughtful use

Fig. 11. Virginia Abutment (Hoppe et al., 2016).

of UWS is recommended based on the guidelines described in the previous section, maintenance painting after decades of service should be anticipated as a potential need. If UWS fails to perform in an acceptable manner in a given situation, AISC (2022) give recommendations for rehabilitating the structure through painting. Situations where this may occur are likely to be ones where painted steel structures would need to be repainted in a similar time frame (and the performance of other material types is uncertain or costlier). Thus, the use of UWS effectively avoids one painting cycle.

CONCLUSIONS

The content of this paper reviews information that can be used to advance considerations of corrosion, which are presently relatively subjective and qualitative, to a more scientifically grounded and data-driven design process. The ultimate vision is to implement the concept of a limit state [which is ubiquitously used for providing sufficient resistance to physical stresses (Eq. 1)] to designing for corrosion, through limit state equations comparing predicted corrosion resistance to the anticipated corrosive effect of the environment (Eq. 2). In terms of predicted corrosion resistance, two categories of information have resulted from the recent research summarized herein. One of these was binary categories of good and inferior corrosion resistance of UWS based on the environment in which it was located. This detailed analysis of UWS is an important focus because of it being the minimum life-cycle cost option in environments where it performs well. The other category of information related to corrosion resistance was relative rankings of the corrosion resistance of other corrosion protection systems. The datasets used to form both of these conclusions were based on long-term, in-situ field performance of real structures, using large national datasets. Ongoing laboratory research will supplement these findings by providing quantitative assessments for different corrosion protection systems in identical environments, which is not possible to do the field.

With respect to quantifying the corrosive effects of environments, the environments of greatest concern to owners have been quantified for UWS but have not been quantified for other materials or corrosion protection systems beyond the relatively coarse considerations shown in Figure 4. One of these is coastal environments. The coastal environments of concern for UWS are limited to the micro-environment of waterway crossings existing in the macro-environments mapped in Figure 7, which are quantitatively described by Table 2. A second environment of concern is highway overpasses in environments where deicing agents are heavily used. The heavy deicing environment for highway overpasses is governed by micro-environment effects (rendering a map an unsuitable descriptor) that are described by Table 3. These conclusions can be thought of as indirect means of summing a set of environmental variables to begin framing corrosion as a limit state. This same approach could be readily applied to gain a similar level of understanding for other corrosion protection systems and/or materials, which would be highly valuable future research. Such analyses should also consider alternative degradation mechanisms for the corrosion protection system or material under evaluation. While corrosion of steel is governed by the "elements" comprising water and chloride, it should be considered that other corrosion protection systems and materials are vulnerable to effects such as those caused by ultraviolet radiation, freeze-thaw cycles, etc.

Lastly, unlike most other limit states where initial design considerations can be relied upon to achieve the limit state, corrosion limit states can be most effectively met through initial design considerations coupled with maintenance practices. This includes practices that increase corrosion resistance and/or decrease the severity of the environment. To achieve appropriate corrosion resistance when the environment is not exceptionally corrosive, the least-cost option of UWS is recommended. However, when the corrosivity of the environment is high, the corrosion resistance can be increased by choosing alternative corrosion protection systems. Alternatively, designers can also decrease the severity of the environment in various ways, with the most impactful option being, in general, detailing the nano-environment (during the initial design) to limit exposure to water and performing periodic inspections and maintenance as needed to maintain adequate protection from and drainage of water. This is true for both bridges and the exposed elements of buildings. Furthermore, during the service life of highway bridges, data demonstrates there is significant benefit to decreasing the severity of the environment through maintenance actions such as joint maintenance and bridge washing. Thoughtful combinations of these strategies allow structures to reach or exceed their targeted lifespans for minimal cost.

ACKNOWLEDGMENTS

This paper represents a written summary of the 2023 American Institute of Steel Construction (AISC) T. R. Higgins Lecture. The honor of this award, and the time that it allowed to synthesize the research reviewed herein into the novel framework proposed, are humbly appreciated. This synthesis is founded on research funded by FHWA (contract 693JJ318F000133) and AISC. The financial support of these organizations and the technical support of their staff that oversaw those projects were vital to the production of this work. However, no formal endorsement of any findings or commentary contained herein is made by these agencies,

with the exception of references made to their publications. Co-investigators for portions of this work were Tripp Shenton, the late Dennis Mertz, Tom Murphy, Travis Hopper, and Ed Wasserman. This work also benefited from the pleasant and informative interactions with Pedro Albrecht, an exceptional role model and bridge corrosion researcher. Field work and data mining efforts for portions of this work were organized through the Long-Term Bridge Performance Program. The state coordinators and their staff that participated in this data collection effort and those that supported the field work through logistical and in-kind support were also invaluable to conducting this research. All of these contributions to this work are gratefully acknowledged.

REFERENCES

AASHTO (2001), *Guide for Commonly Recognized (CoRe) Structural Elements: 2002 Interim Revisions,* American Association of State Highway and Transportation Officials, Washington, D.C.

AASHTO (2011), *Guide Manual for Bridge Element Inspection*, American Association of State Highway and Transportation Officials, Washington, D.C.

AASHTO (2019), *Manual for Bridge Element Inspection*, 2nd Ed., American Association of State Highway and Transportation Officials, Washington, D.C.

AASHTO (2020), *Guide Specification for Service Life Design of Highway Bridges*, American Association of State Highway and Transportation Officials, Washington, D.C.

AASHTO (2021), *Standard Specifications for Transportation Materials and Methods of Sampling and Testing and Provisional Standards*, 41st Ed., American Association of State Highway and Transportation Officials, Washington, D.C.

AASHTO (2023), "A User's Guide to Bridge Cleaning," AASHTO Transportation System Preservation Technical Services Program, retrieved from https://tsp2bridge.pavementpreservation.org/technical/fhwa/pocket-guides/, last accessed December 7, 2023.

AISC (2022), *Uncoated Weathering Steel Reference Guide*, American Institute of Steel Construction, Chicago, Ill.

Albrecht, P., Coburn, S.K., Wattar, F.M., Tinklenberg, G.L., and Gallagher, W.P. (1989), "Guidelines for the Use of Weathering Steel in Bridges," NCHRP report 314, Transportation Research Board, National Research Council, Washington, D.C.

ASTM (2019), "Standard Specification for High-Strength Low-Alloy Structural Steel, Up to 50 ksi [345 MPa] Minimum Yield Point, with Atmospheric Corrosion Resistance," A588-19, ASTM International, West Conshohocken, Pa.

ASTM (2021), "Standard Specification for Structural Steel for Bridges," A708-21, ASTM International, West Conshohocken, Pa.

Chase, S. (2012), Personal communication.

FHWA (1989), "Uncoated Weathering Steel in Structures," Technical Advisory 5140.22, Federal Highway Administration, Washington, D.C. Updated 2017.

FHWA (1995), "Recording and Coding Guide for the Superstructure Inventory and Appraisal of the Nation's Bridges," report FHWA/PD-96/001, Federal Highway Administration, Office of Engineering, Bridge Division, Bridge Management Branch, Washington, D.C.

FHWA (2022), "Download NBI ASCII Files," https://www.fhwa.dot.gov/bridge/nbi/ascii.cfm, last accessed May 17, 2023.

Hoppe, E., Weakley, K., and Thompson, P. (2016), "Jointless Bridge Design in the Virginia Department of Transportation," *Transportation Research Procedia* 14, pp. 3,943–3,952.

Hopper, T., Langlois, A.-M., and Murphy, T. (2022), *Service Life Design Reference Guide*, Federal Highway Administration, Washington, D.C.

ISO (1988), "Corrosion of Metals and Alloys—Classification of Corrosivity of Atmospheres," Draft Proposal DP 9224, International Organization of Standardization, Geneva, Switzerland.

ISO (2012), "Corrosion of Metals and Alloys—Corrosivity of Atmospheres—Classification, Determination and Estimation," ISO 9223:2012, International Organization of Standardization, Geneva, Switzerland.

Kogler, R. (2015), "Corrosion Protection of Steel Bridges," *Steel Bridge Design Handbook*, Vol. 19, report FHWA-HIF-16-002, Federal Highway Administration, Washington, D.C.

McConnell, J., Chan, C., Giannino, J., and Young, N. (2022), "Durability of Steel Bridge Corrosion Protection Systems Using Environment-Based Accelerated Corrosion Testing," American Institute of Steel Construction, Chicago, Ill.

McConnell, J., Shenton, H., Bai, T., and Rupp, J.T. (2024), "Weathering Steel Performance Data Collection," U.S. Department of Transportation, Federal Highway Administration, Washington, D.C.

Milner, M.H. and Shenton, H. (2014), "Survey of Past Experience and State-of-the-Practice in the Design and Maintenance of Small Movement Expansion Joints in the Northeast," AASHTO Transportation System Preservation Technical Services Program (TSP2); http://sites.udel.edu/dct/research/publications/soils-structures-and-bridges/, last accessed December 5, 2023.

NACE (2016), "NACE International Impact Study," NACE International, http://impact.nace.org/, last accessed December 7, 2023.

NADP (2020), "National Atmospheric Deposition Program 2019 Annual Summary," Wisconsin State Laboratory of Hygiene, University of Wisconsin–Madison, Madison, Wis.

NIBS (2023), "Corrosion Maps," https://www.wbdg.org/additional-resources/tools/corrosion-toolbox/maps, last accessed December 5, 2024.

Behavior of Extended Single-Plate Shear Connections Subjected to Combined Shear and Compression Forces Using Finite Element Analysis

SUNIL SAPKOTA, GIAN ANDREA RASSATI, JAMES A. SWANSON, and BO DOWSWELL

ABSTRACT

Extended single-plate shear connections can be subjected to compression loads in addition to shear loads during extreme events like wind and earthquakes. However, the existing interaction equations found in the AISC *Steel Construction Manual* (2023), in literature, and in design examples—which are being used in design for combined loading cases—have not been formally validated for use by experimental testing or finite element analysis. This research aims to study the behavior of these connections when subjected to combined loading of shear and compression force by performing a nonlinear finite element analysis in ABAQUS (2022). The variables considered in the study are column web stiffness, connection configurations, and different bracing conditions of the beam. The results from these analyses were compared to the available interaction equations in the AISC *Manual* and in literature to assess their applicability under different conditions. Shear-compression interaction plots were generated from the results that show the shear strength decreases with an increase in compression force in the connection. The effect of the compression force on the shear strength depends on the column web's rigidity and the bracing condition of the beam.

Keywords: extended shear tabs, finite element analysis (FEA), combined loading, compression, shear, interaction equations.

INTRODUCTION

Single-plate shear connections offer many advantages over other connection configurations: They are cost effective, are easy to fabricate, and provide rapid erection capabilities. However, when the supported beam needs to be connected to the web of the girder or the web of the supporting column, the ends of the beam may need to be coped as shown in Figure 1(a). Coping makes the fabrication process difficult and expensive, which takes away the advantages that these connections offer.

Coping can be avoided by extending the plate beyond the flange of the supporting column or girder. This causes the *a* distance [the distance between weld line and bolt line as shown in Figure 1(a)] to be longer than the limit set for conventional shear tabs; such configuration of the shear tab is known as extended single-plate shear connection, or extended shear tab, and is shown in Figure 1(b). The major benefit of these connections is that the fabrication process is simple, and erection work is faster as coping of the beam is avoided. Owing to the larger length compared to conventional shear tabs, they have higher eccentricity, resulting in a higher moment in the connection. This makes the behavior of extended shear tabs different than the conventional configurations, resulting in additional failure modes and limit states that need to be considered.

Two types of conceptual support conditions may exist for these connections—rigid and flexible. When a shear tab is attached to the column flange or connected to both sides of the girder or column web, the support is considered rigid (Muir and Hewitt, 2009). The extended shear tabs that are connected on only one side of the column web or girder web are considered to have a flexible support condition. The support condition affects the behavior of these connections as it influences the point of inflection of the in-plane moment, which ultimately affects the moment to which the bolt group is subjected. In some extended shear tabs, stabilizer plates are provided to improve the stability of the connection as shown in Figure 2. These configurations are called stiffened extended shear tabs, and the ones without any stabilizer plates are called unstiffened extended shear tabs.

The actual moment developed in the plate and bolt group is difficult to estimate because there is an uncertainty in the actual rigidity of the supports, and it is difficult to find the exact stiffness of the connection. Research done in the

Sunil Sapkota, Graduate Structural Engineer, JPS Consulting Engineers LLC, Indianapolis, Ind. Email: sunil@jpsconsultingengineers.com

Gian Andrea Rassati, PhD, Associate Professor, Department of Civil and Architectural Engineering and Construction Management, University of Cincinnati, Cincinnati, Ohio. Email: rassatga@ucmail.uc.edu (corresponding)

James A. Swanson, PhD, Associate Professor, Department of Civil and Architectural Engineering and Construction Management, University of Cincinnati, Cincinnati, Ohio. Email: swansojs@ucmail.uc.edu

Bo Dowswell, PhD, PE, Principal, ARC International, LLC, Birmingham, Ala. Email: bo@arcstructural.com

Paper No. 2024-02

past has focused on the study of failure modes, shear load eccentricity, support rotation, and stability of the extended shear tabs. Most of the studies were focused on the case of gravity-induced shear load alone. However, in certain cases connections are expected to carry axial load as well as shear load, and their combined presence will affect the behavior of the connection. One of the most common sources of axial load in connections is lateral load (wind or earthquake load). Axial load is developed in the connection when a supported member is a part of the lateral load-resisting path. Similarly, for gable-shaped buildings, axial forces can be developed in the connection. Furthermore, an extreme load

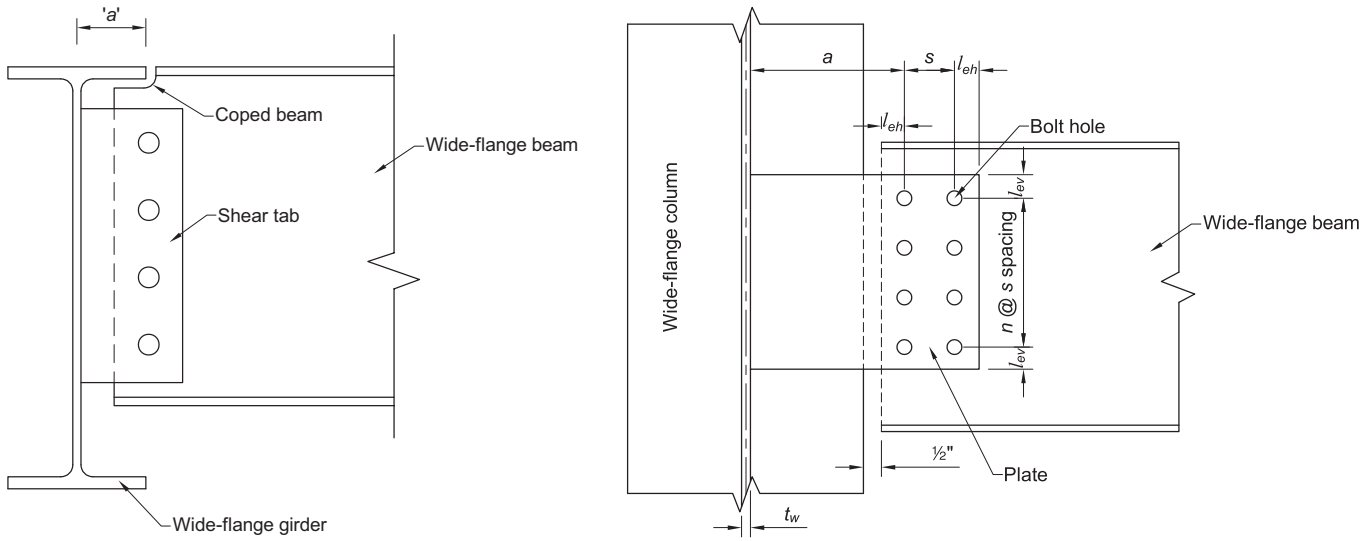

(a) Coped beam-to-girder connection (Asl et al., 2019) *(b) Unstiffened extended single-plate shear connection*

Fig. 1. Single-plate shear connections.

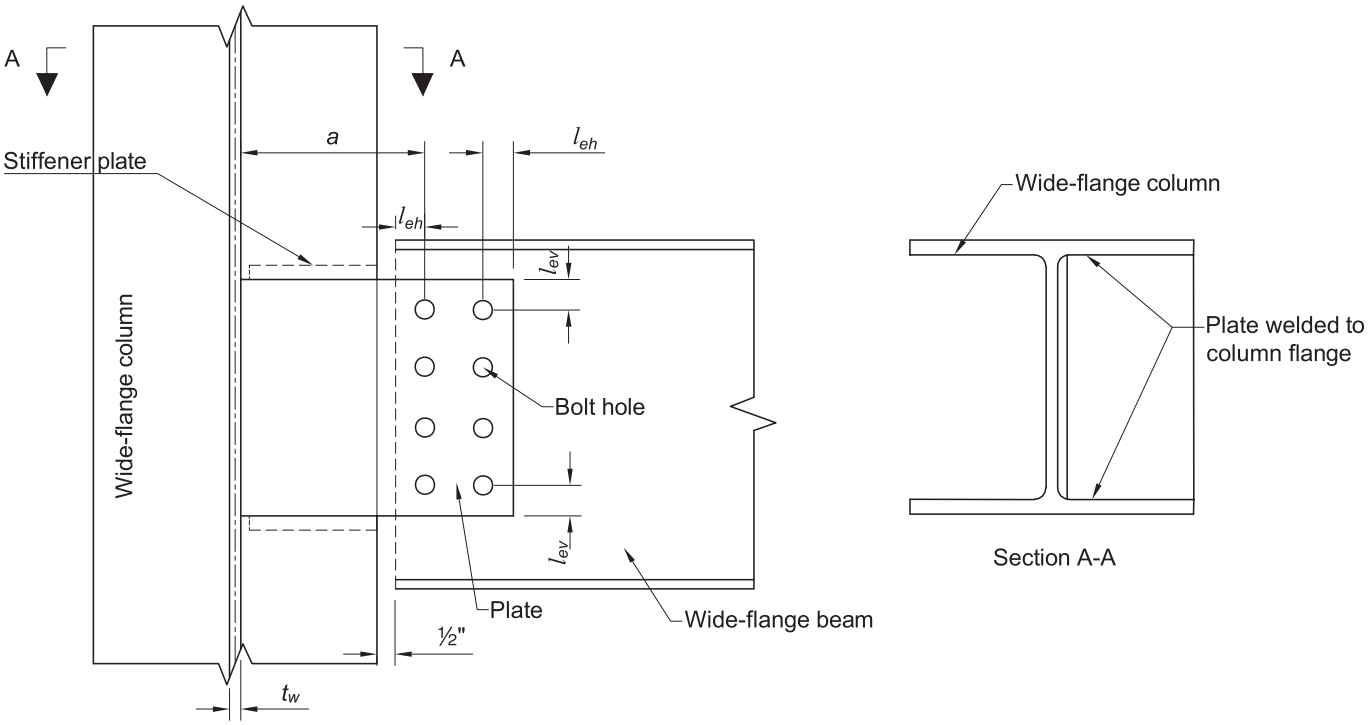

Fig. 2. Stiffened extended shear tab connected to column web.

event such as a blast or a fire may lead to the development of axial forces that will need to be transferred through the connection, due, for example, to the emergence of catenary action in the beam or to the loss of a column. There are very few studies that examine the behavior of these connections under combined shear and axial forces. This research focuses on the study of the behavior of unstiffened extended shear tabs connected to the web of a column under a combined loading of shear and axial compression forces.

BACKGROUND

Past Research on Combined Loading

Mirzaei (2014) conducted four full-scale experimental tests of conventional shear tabs for combined loading of shear and axial force in order to improve the design procedure for shear tabs in Canadian specifications. The experimental testing was followed by a parametric study in ABAQUS (2022), which showed that adding a small compression load increased the shear strength, but beyond a certain range, the strength decreased. Conversely, the addition of tensile force decreased the shear strength. This behavior was attributed to the compression load delaying the weld tearing, while the addition of tensile load put higher demands on the weld, resulting in weld failure.

Thomas (2014) performed full-scale testing on 23 extended shear tabs, 12 of which were subjected to combined loading of shear and axial forces. The major parameters studied were tab depth, tab thickness, and presence of stiffeners. The support condition was flexible because the plates were welded single sided to a web of a column stub. The failure mode for tensile loading was weld rupture, while for compression loading it was bolt fracture. The addition of axial load decreased the shear strength, and this effect was more pronounced for tensile loading and deeper connections.

Salem (2016) conducted experimental and finite element analysis (FEA) with both semi-rigid and rigid support conditions. It was observed that for a rigid support condition, an increase in compression force caused a rapid decrease in shear strength. On the other hand, for a semi-rigid support, the addition of compression increased the strength. However, it should be noted that testing was done for only one level of compression load, so no definitive conclusions can be drawn about the actual behavior under combined loading.

Nasrabadi (2018) conducted experimental and FEA on various cases of extended shear tabs, including the unstiffened configuration. The results revealed that the application of axial compression either decreased or increased the ultimate strength of the connections, depending on the intensity of the axial force and on the mode of failure experienced under the application of a pure shear load. Conversely, the application of axial tension decreased the strength in all cases. For a connection whose failure mode was buckling under shear load alone, its strength decreased. However, for a connection with net section rupture as the failure mode, its strength increased for a level of force up to 37% of the axial yield strength.

AVAILABLE INTERACTION EQUATIONS FOR DESIGN UNDER COMBINED SHEAR AND AXIAL FORCES

There are several interaction equations in the 16th Edition of the AISC *Steel Construction Manual* (2023), hereafter referred to as the AISC *Manual*. The first, AISC *Manual* Equation 10-8, shown as Equation 1, includes only the interaction of shear and flexural yielding. It does not include the case of axial loading. The second, AISC *Manual* Equation 9-1, shown as Equation 2, is included for the interaction of shear, moment, and axial load for the case of in-plane loading only. Design considerations for extended single-plate shear connections subjected to combined shear and axial forces have been incorporated in the newly added Part 12 of the AISC *Manual*, which suggests using Equations 12-2 and 12-3 to check the plate for the interaction of axial force (tension and compression), shear force, and flexure for yielding and lateral torsional buckling. These equations, listed as Equations 3 and 4, are derived from AISC *Specification for Structural Steel Buildings* (AISC, 2022a) Chapter H, in conjunction with AISC *Manual* Equation 10-8. They include the minor-axis flexural term, wherein the required flexural strength is calculated by using the geometric horizontal eccentricity. Additionally, the AISC *Manual* suggests that the weak-axis flexural term need not be included in the strength check whenever a slab is present at the top of the supported beam and there is sufficient restraint against the rotation about its longitudinal axis. The use of these equations can be found in the AISC *Companion to the Steel Construction Manual*, Example IIA-19B (2022b), to check for the interaction of axial, shear, and flexural yielding of the plate, as well as rupture of the plate. It assumes the case where a slab is present at the top of the beam, providing sufficient restraint against minor-axis rotation, and completely ignores the minor-axis flexural term in the equation. Equations 3 and 4 will take the form of Equations 5 and 6 when the weak-axis flexural term is ignored in the equation.

None of the AISC *Manual* equations have included torsional load into the interaction equations applicable to extended shear tabs. Dowswell (2019) proposed an interaction equation for an extended shear tab under combined loading by explicitly including the torsional term, as shown in Equation 7. This equation also uses geometric

eccentricity to calculate the torsional moment. However, no experimental or finite element studies have been performed to validate the effectiveness of these equations in predicting the strength of extended shear tabs subjected to combined shear and axial force.

$$\left(\frac{V_r}{V_c}\right)^2+\left(\frac{M_r}{M_c}\right)^2\le 1.0 \tag{1}$$

$$\frac{M_r}{M_c}+\left(\frac{P_r}{P_c}\right)^2+\left(\frac{V_r}{V_c}\right)^4\le 1.0 \text{ for } \frac{P_r}{P_c}<0.2 \tag{2}$$

$$\left(\frac{P_r}{2P_c}+\frac{M_{rx}}{M_{cx}}\right)^2+\left(\frac{V_r}{V_c}\right)^2\le 1.0 \text{ for } \frac{P_r}{P_c}<0.2 \tag{3}$$

$$\left(\frac{P_r}{2P_c}+\frac{8}{9}\frac{M_{rx}}{M_{cx}}\right)^2+\left(\frac{V_r}{V_c}\right)^2\le 1.0 \text{ for } \frac{P_r}{P_c}\ge 0.2 \tag{4}$$

$$\left[\frac{P_r}{2P_c}+\left(\frac{M_{rx}}{M_{cx}}+\frac{M_{ry}}{M_{cy}}\right)\right]^2+\left(\frac{V_r}{V_c}\right)^2\le 1.0 \text{ for } \frac{P_r}{P_c}<0.2 \tag{5}$$

$$\left[\frac{P_r}{2P_c}+\frac{8}{9}\left(\frac{M_{rx}}{M_{cx}}+\frac{M_{ry}}{M_{cy}}\right)\right]^2+\left(\frac{V_r}{V_c}\right)^2\le 1.0 \text{ for } \frac{P_r}{P_c}\ge 0.2 \tag{6}$$

$$\left(\frac{P_r}{P_c}\right)^k+\left(\frac{T_r}{T_c}\right)^2+\left(\frac{V_r}{V_c}\right)^4+\left[\left(\frac{M_{rx}}{M_{cx}}\right)^{1.7}+\left(\frac{M_{ry}}{M_{cy}}\right)^{1.7}\right]^{0.59}\le 1.0 \tag{7}$$

$$M_{ry}=P_r\left(\frac{t_p+t_w}{2}\right) \tag{8}$$

where

$k = 1$ for compressive load
$= 2$ for tensile load

RESEARCH SIGNIFICANCE

Based on the literature study, it was found that there are only a few research programs that have been conducted to study the behavior of extended shear tabs subjected to combined shear and axial forces. The studies done in the past were mostly qualitative in nature where the specimens were not subjected to a range of axial loads. The available results from past research programs show that axial load will influence the ultimate strength and failure mode of the connection. The AISC 15th Edition *Manual* (2017) did not include the case of axial loading in the design procedure for extended shear tabs. The newly added Part 12 in the AISC 16th Edition *Manual* (2023) now includes Equations 5 and 6 to consider the interaction of shear, axial, and flexural forces. However, no experimental and analytical studies have been performed to validate the use of these equations. This study aims to understand the behavior of extended shear tabs subjected to combined shear and compression forces and validate the use of these interaction equations.

Finite element analyses by Rahman et al. (2007) identified the relevant parameters, such as the coefficient of friction, boundary conditions, element types, and loading steps for finite element modeling of extended shear tabs. The work done by Thomas (2014), Salem (2016), and Nasarbadi (2018) concluded that finite element models can accurately predict the results of the experimental testing done in extended shear tabs subjected to combined loading of shear and compression forces as well. Because experimental testing for the case of combined loading is very difficult and expensive, finite element analysis is a valuable tool to study the behavior of extended shear tabs under combined shear and compression forces.

TEST MATRIX AND FINITE ELEMENT ANALYSIS

Test Matrix

Table 1 shows the test matrix that was developed to study the behavior of the extended shear tabs subjected to combined shear and compression forces. The test matrix was developed based on commonly used practical connection components. The three major variables are column web stiffness, connection configuration, and lateral bracing condition of the beams. For each of the connection configurations, the size of the beams, plate thickness, and depth of the plate were made constant.

Figures 3, 4, and 5 show the three connection configurations contained in the test matrix. The two columns selected for the study were W14×233 and W14×90. They are representative of columns used for heavy loads and light loads, respectively, and also provide a range of support condition flexibility. Each 10-ft-long column was connected to three different beam sizes through three different connection configurations. Each case was analyzed for three different practical beam bracing conditions, for a total of 18 cases. Connections 1 and 4, 2 and 5, and 3 and 6 are identical to each other, with the exception of the column size.

Finite Element Modeling in ABAQUS

Previous work by the authors (Ruffley, 2011; Ganaganur Anantharam, 2022) amply demonstrated the capabilities of the finite element modeling approach employed in this work, as also supported by Rahman et al. (2007), among many. The following provides a detailed summary of the modeling approach employed.

Table 1. Test Matrix				
Column Size	**Beam Size**	**Connection ID**	**Connection Configuration**	**Bracing Condition of the Beam**
W14×90	W14×30 Length = 21 ft	Connection 1	3 rows of 2 bolts (total of 6 bolts), ⅜ in. plate	i. Top flange continuously braced ii. One-point lateral restraint on top flange near the connection end iii. No lateral restraint on top flange
	W18×35 Length = 27 ft	Connection 2	4 rows of 2 bolts (total of 8 bolts), ½ in. plate	i. Top flange continuously braced ii. One-point lateral restraint on top flange near the connection end iii. No lateral restraint on top flange
	W24×76 Length = 36 ft	Connection 3	5 rows of 2 bolts (total of 10 bolts), ⅝ in. plate	i. Top flange continuously braced ii. One-point lateral restraint on top flange near the connection end iii. No lateral restraint on top flange
W14×233	W14×30 Length = 21 ft	Connection 4	3 rows of 2 bolts, (total of 6 bolts) ⅜ in. plate	i. Top flange continuously braced ii. One-point lateral restraint on top flange near the connection end iii. No lateral restraint on top flange
	W18×35 Length = 27 ft	Connection 5	4 rows of 2 bolts (total of 8 bolts), ½ in. plate	i. Top flange continuously braced ii. One-point lateral restraint on top flange near the connection end iii. No lateral restraint on top flange
	W24×76 Length = 36 ft	Connection 6	5 rows of 2 bolts (total of 10 bolts), ⅝ in. plate	i. Top flange continuously braced ii. One-point lateral restraint on top flange near the connection end iii. No lateral restraint on top flange

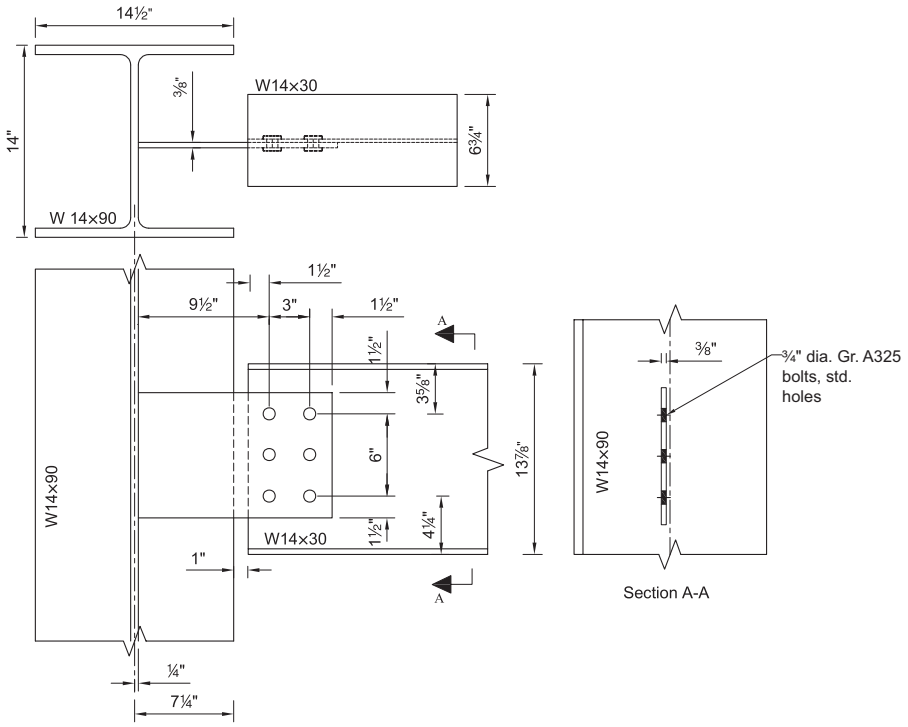

Fig. 3. Connection configuration 1.

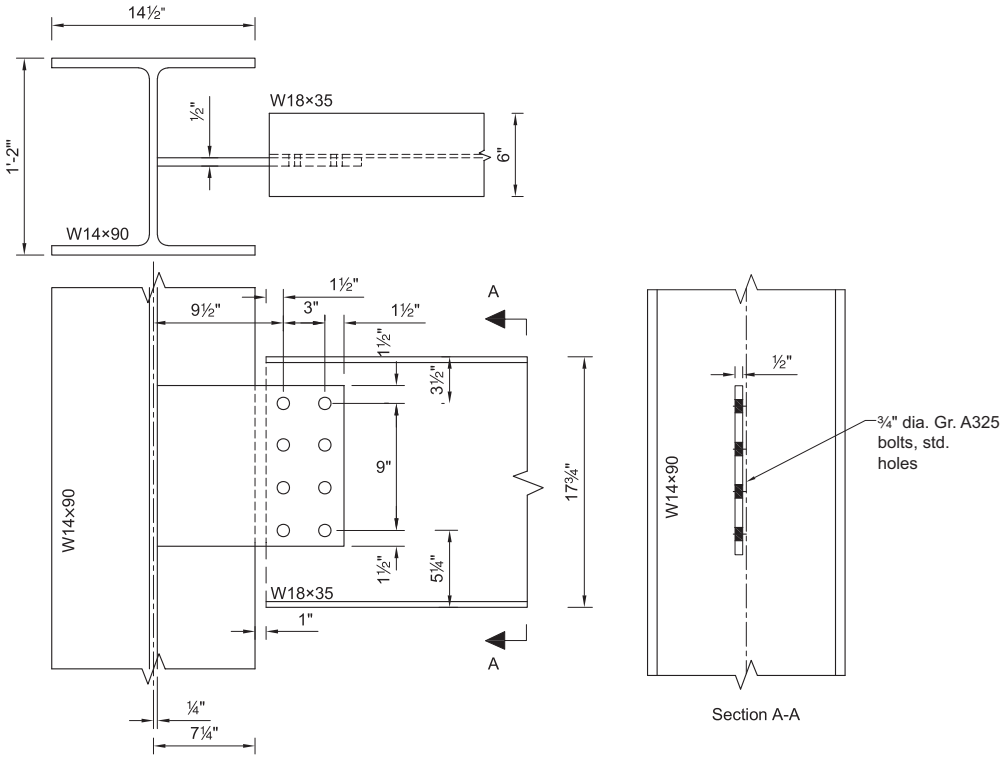

Fig. 4. Connection configuration 2.

Parts, Partitions, Assembly, and Meshing

Parts were created in ABAQUS for each component of a connection using the geometric properties provided in the AISC *Manual* (2017). Partitioning for beams, columns, bolts, and plates was done to achieve a better mesh quality. Beams were modeled only up to half of their length by applying a symmetric restraint at the midspan. To achieve a finer mesh near the connection end and a coarser mesh elsewhere, two separate parts of the beam were created: one with a length equal to twice the depth of the beam, d_b, and other for the remaining length. These parts were then connected using a tie constraint. The same process was followed for the column. The mesh size used in the model is shown in Table 2.

Material Properties

The material model for the beam, column, and plate was taken from the experimental data of past coupon testing done at the University of Cincinnati for an unrelated project, which is shown in Table 3. The tested coupon was ASTM A572/A572M Gr. 50 (2021) steel and was used for both the shear plate and the I-shapes. The measured tensile yield stress and tensile strength were 55.1 ksi and 67.4 ksi, respectively. Similarly, Table 4 shows the material model for bolts that was taken from experimental bolt testing done at the University of Cincinnati. The tested bolts material was ASTM F3125 Gr. A325 (2023) with an ultimate strength of 120 ksi. The measured tensile yield stress and tensile strength were 99.0 ksi and 130 ksi, respectively.

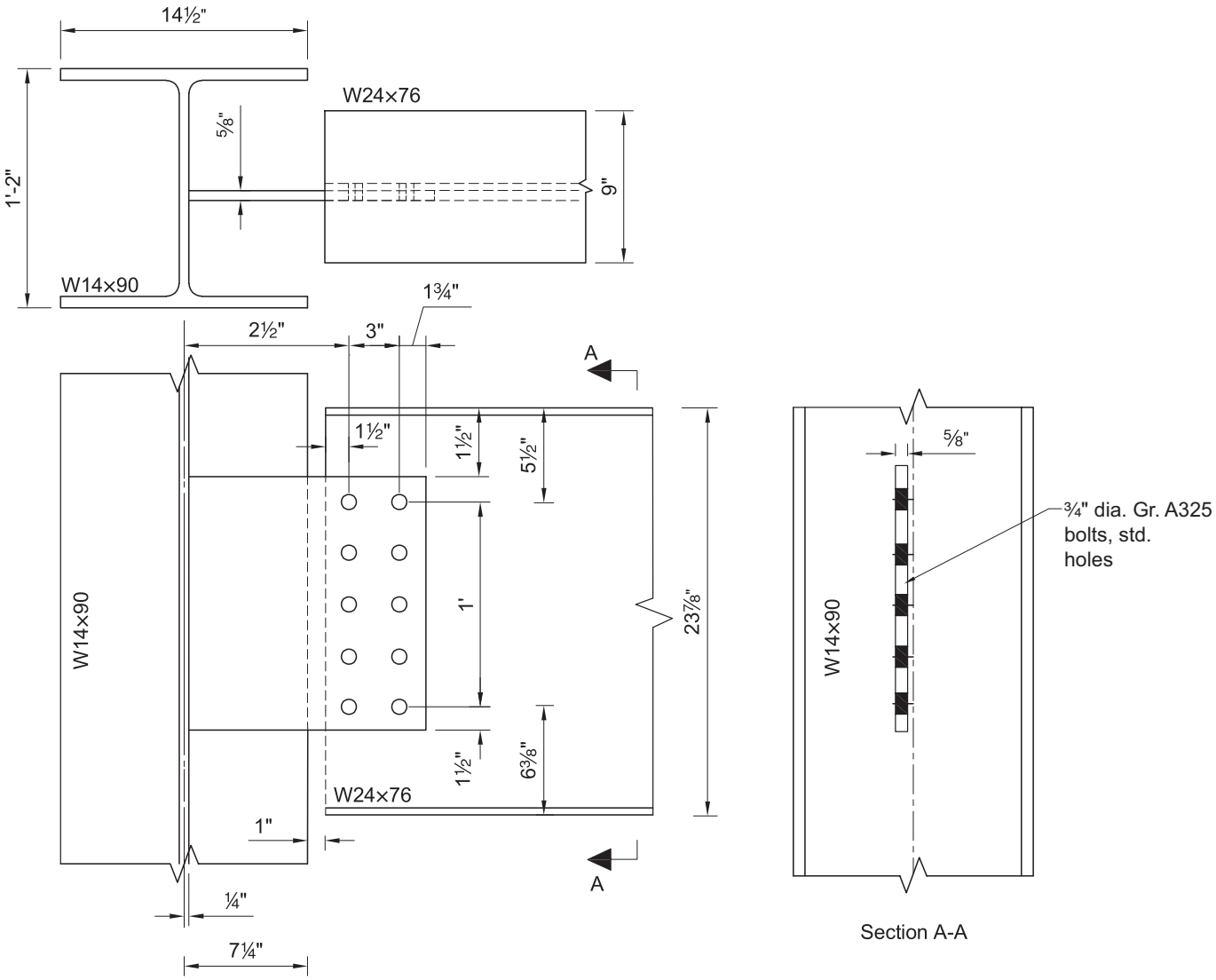

Fig. 5. Connection configuration 3.

Table 2. Mesh Size		
Connection Component	**Partitions**	**Mesh Size, in.**
Beam	$2d_b$ distance	0.2
	Remaining length	0.8
Columns	$3d_b$ distance	0.2
	Remaining length	0.8
Bolts		0.07
Plates		0.15

Table 3. Material Properties for ASTM A572/A572M Gr. 50 and ASTM A992/A992M (2022) Steel				
Engineering Stress, ksi	**Engineering Strain**	**True Stress, ksi**	**True Strain, (in./in.)**	**Plastic Strain (in./in.)**
0	0	0	0	0
55.1	0.00175	55.1	0.00175	0
55.0	0.0305	56.7	0.0300	0.028296
60.5	0.0500	63.5	0.0488	0.047042
65.7	0.100	72.3	0.0953	0.093562
67.0	0.150	77.1	0.140	0.138013
67.4	0.200	80.9	0.182	0.180573
66.5	0.250	83.1	0.223	0.221395
61.7	0.300	80.2	0.262	0.260616
44.3	0.350	59.8	0.300	0.298356
0.0	0.350	0.0	0.300	0.298357

Table 4. Material Properties for ASTM F3125 Gr. A325 Bolts				
Engineering Stress, ksi	**Engineering Strain (in./in.)**	**True Stress, ksi**	**True Strain (in./in.)**	**Plastic Strain (in./in.)**
0	0	0	0	0
99.1	0.00256	99.3	0.00255	0
114.3	0.00704	115.1	0.00701	0.00446
120.7	0.02333	123.6	0.0231	0.0205
128.4	0.04039	133.6	0.0395	0.0370
130.0	0.06315	138.2	0.0612	0.0587
119.1	0.12577	135.1	0.118	0.116
99.2	0.18271	117.3	0.168	0.165
80.3	0.22200	98.2	0.200	0.198

Contact Interaction

Contact interaction among the bolts, plate, and beam web was simulated by creating a contact pair and assigning a interaction property to each contact pair for both normal and tangential behavior. Based on the research of Rahman et al. (2007), the coefficient of friction assigned for tangential behavior was 0.3. "Hard contact" was assigned as the normal behavior.

Based on the study by Ruffley (2011), 3D solid, first-order elements have been used in this work. Reduced integration was used instead of fully integrated first-order elements to avoid the stiff response of the elements in bending, which is known as "shear locking." However, first-order linear elements with reduced integration (C3D8R) are sensitive to hour-glassing; the effect resulting in elements with no stiffness when subjected to bending (Mirzaei, 2014). ABAQUS has hourglass control available to reduce this effect. Taking all of these into consideration, the element type used in the analysis was a 3D solid, linear brick element with reduced integration and hourglass control.

Restraints, Constraint, Analysis Step, and Loading

A reference point was provided at the centroid of the end surface of the beam and column. The nodes of the end surface of the beam and column were coupled to the respective reference point by using a kinematic coupling constraint. The boundary conditions and load were then applied to the reference point. The weld between the plate and the column web was not explicitly modeled. The weld's behavior was simulated by using a tie constraint between the plate end surface (slave surface) and the column web surface (master surface). The displacement at the column ends was restrained in all three directions, and rotation was restrained about the longitudinal axis of the column. The beam free end was provided with a XSYM (U1 = UR2 = UR3 = 0) boundary condition enforcing symmetry in a plane transverse to the axis of the beam.

In addition, to prevent lateral buckling failure of the beams under compressive load, lateral restraints were applied. The W14×30 beam was restrained at two points, the W18×35 at four points, and the W24×76 at three points along the span at a uniform spacing. To achieve a lateral restraint in ABAQUS, the beams were divided into the number of parts equal to the required number of bracings to create a set of nodes. Then, the appropriate boundary condition was applied to the nodes on each division. The number of bracing points was fixed to prevent lateral buckling and to maintain a consistent ratio of L_b/r_y (L_b = unbraced length, and r_y = radius of gyration about the weak axis) for all beams. Similarly, for compression loading, flange buckling was observed in the W14×90 column. Therefore, the flanges of the W14×90 column were restrained in the lateral direction at all nodes along the column flanges to prevent local buckling of the column, which was outside of the scope of this study.

Compressive loading was applied to the beam end, while shear loading was applied as a point load at such a distance from the connection end as to obtain the same shear force and rotation that would be produced by applying a uniformly distributed load over the span. To prevent the lateral torsional buckling failure of the beam, loads were applied 2 ft away from the connection in the beam bracing cases where the top flange is not continuously restrained in the lateral direction.

Loading was applied in two steps—pretensioning and loading—whenever an analysis was run for the case of shear load only. However, when the compression load was included in the analysis, the loading was applied in five steps. The loading protocol for the horizontal loading was taken from research by Mirzaei (2014) where at first the shear load was applied as a displacement-based vertical load up to the service level. After that, the desired compression force (as a percentage of the axial yield strength of the plate) was applied in full as a point load (force-based loading). Finally, the remaining shear load was applied up to failure, keeping the axial load constant.

All analysis steps included geometric nonlinearity. The direct equation solver was used with Full Newton Raphson as the solution technique. The steps in the analysis are further explained in the following:

i. Initial Step

In this step, restraints were applied to the ends of the beam and column. No external load was applied in this step.

ii. Pretensioning Step

In this step, bolts were pretensioned using the temperature method based on the research of Ruffley (2011). Additionally, Ganaganur Anantharam's (2022) research work shows that the temperature method for bolt pretensioning can simulate the most realistic behavior of the pretensioned bolt in all conditions up to failure. In this method, a temperature decrease was applied to the shank of each bolt to achieve the minimum pretension force specified in AISC *Specification* Table J3.1. For ¾-in.-diameter ASTM F3125 Gr. A325 bolts, the minimum pretension force required is 28 kips. The bolts used in the model had threads excluded from the shear plane. The temperature decrease required to achieve this minimum pretension is given by Equation 9. However, this is strictly true only if the materials in the grip are perfectly rigid. So, this equation is only capable of providing an initial estimate of the temperature change required. Following that, a

series of iterations must be performed, decreasing the temperature each time until the required pretension is achieved.

$$\Delta T = \frac{P_b}{E\alpha A_b} \tag{9}$$

where ΔT is the temperature change, P_b is the minimum pretension force, E is the modulus of elasticity of steel = 29,000 ksi, A_b is the area of the bolt shank and α is the coefficient of thermal expansion for steel = $6.6 \times 10^{-6}/°F$. The temperature change required to achieve minimum pretension for a bolt used in the analysis using Equation 10 was found to be 331°F, which was used as an initial estimate of the iterative process. Finally, after several iterations, the temperature change that provides the minimum required pretension was found to be −645°F.

iii. Shear Loading–1

In this step, displacement-based vertical loading was applied to the point of shear loading. Whenever the analysis was performed for the case of combined shear and compression, the shear load was applied only up to the service load level. However, if an analysis was performed for the case of shear load alone, loading was applied up to the failure point of the connection in this step and no further loading step was required.

iv. Notional Load

Geometric imperfections were simulated using the notional load approach. Dowswell (2016) discusses the notional load approach to evaluate the stability of gusset plates. A similar approach has been used in this study. The notional load parameter, ξ, was taken as 0.012. A notional load equal to the required axial strength multiplied by the notional load parameter is applied at the first vertical bolt line in the transverse direction. This load is kept constant for the remainder of the loading step.

v. Compression Loading

In this step, compression load was applied to the reference point attached to the end cross section of the beam as a force-based loading. It was applied as the percentage of the axial yield strength of the plate, P_y. The shear load applied up to the service load level was maintained in this step.

vi. Shear Loading–2

In this step, the remaining shear load was applied to the point of shear loading as a displacement-based loading keeping the compression load constant until failure.

RESULTS AND DISCUSSIONS

In the following section, the results and discussion for the finite element analysis of the connections in the test matrix are presented separately for the three different bracing conditions of the beam.

Beam Bracing Case: Top Flange Continuously Braced

The behavior of the connections was dependent on the column size used when subjected to shear loading. The connection with a W14×90 column showed yielding of the plate at the first vertical bolt line, followed by yielding near the support line, as shown in Figure 6. The figure shows the equivalent plastic strain (PEEQ) in the plate, column web, and beam web, where the light gray color indicates yielding. Significant yielding and rotation of the column web were observed. This caused the point of inflection, initially located between the bolt line and the support line, to further shift toward the support line, which increased the moment at the first vertical bolt line and caused yielding at that location.

All connections with W14×90 column showed similar behavior, except for Connection 3, in which bolt failure occurred before the plate reached net section yielding at the first vertical bolt line. This could be attributed to the use of the actual plate thickness of 0.625 in., which was close to the maximum allowable thickness of 0.63 in. as determined by the AISC (2017) design procedure. The bolt failure occurred at a load of 142 kips, which is 1.21 times the strength obtained by using the design procedure of the AISC 15th Edition *Manual* (2017).

In contrast, the connection with a W14×233 column showed yielding of the gross section near the support line first, followed by yielding of the net section at the first vertical bolt line, as shown in Figure 7. Significant yielding and rotation of the column web were not observed. Large out-of-plane deformation at the bottom of the plate was observed due to the higher negative moment in the plate caused by the stiffer column web.

After analyzing the shear loading case, the connections were subjected to pure compression loading to determine the strength of the plate. To apply a compression load, a displacement was provided at the end of the beam in the negative x-direction. The connections failed due to buckling of the plate.

Once the compressive strength of the plate was determined, the connection was subjected to combined shear and compression forces. The connections were analyzed separately for three cases: shear load plus compression force equal to 25%, 50%, and 75% of the total compressive strength obtained from the previous analysis. The application of compressive forces decreased the shear strength of the plate. The failure mode was lateral buckling of the plate.

The force-displacement plot for shear loading and combined loading cases for Connection 1 is shown in Figure 8. The behavior was further studied by generating an interaction plot, which was normalized against the shear yield strength and axial yield strength of the plate as shown in Figure 9.

The comparison of interaction plots for two different columns is shown in Figures 10 and 11. The figures show that at the lower level of compression force, the rate of decrease in shear strength for the rigid support is greater than that for the flexible support. The reason for the higher effect of the compression force on connections with the W14×233 column is the higher negative moment that develops in the connection caused by the rigidity of the column web. This higher negative moment leads to a higher compression force at the bottom of the plate, which interacts with the applied compression force, ultimately resulting in a buckling failure of the plate. At a higher level of compression force, its effect is seen more for a flexible support. However, in the case of Connection 6, its behavior is similar to that of the connection with the W14×90 column.

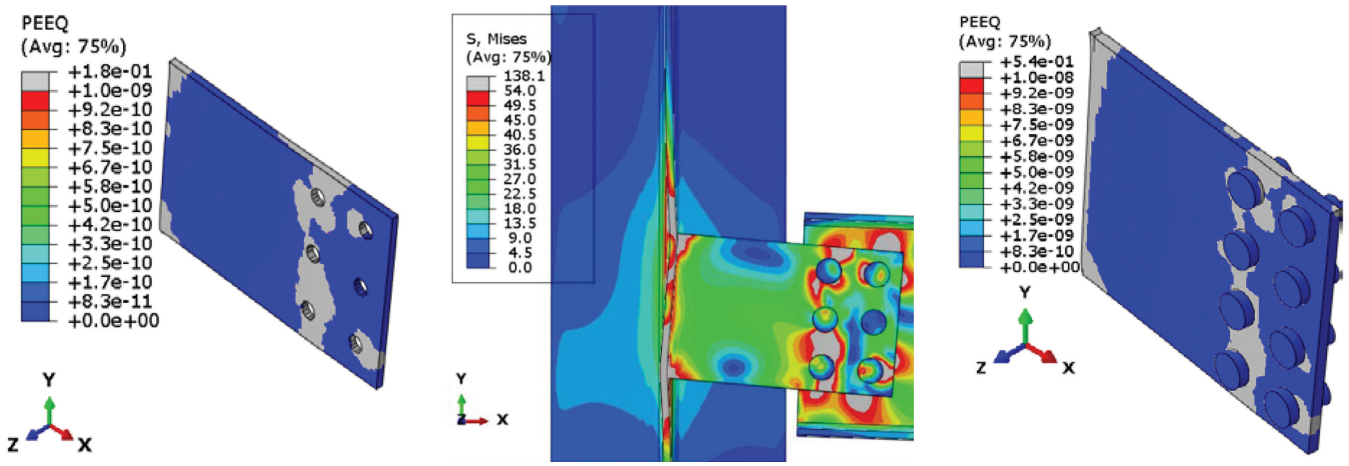

(a) Yielding at net section, Connection 1

(b) Rotation and yielding of column web, Connection 1

(c) Yielding at gross section, Connection 2

Fig. 6. Behavior of connections with W14×90 column.

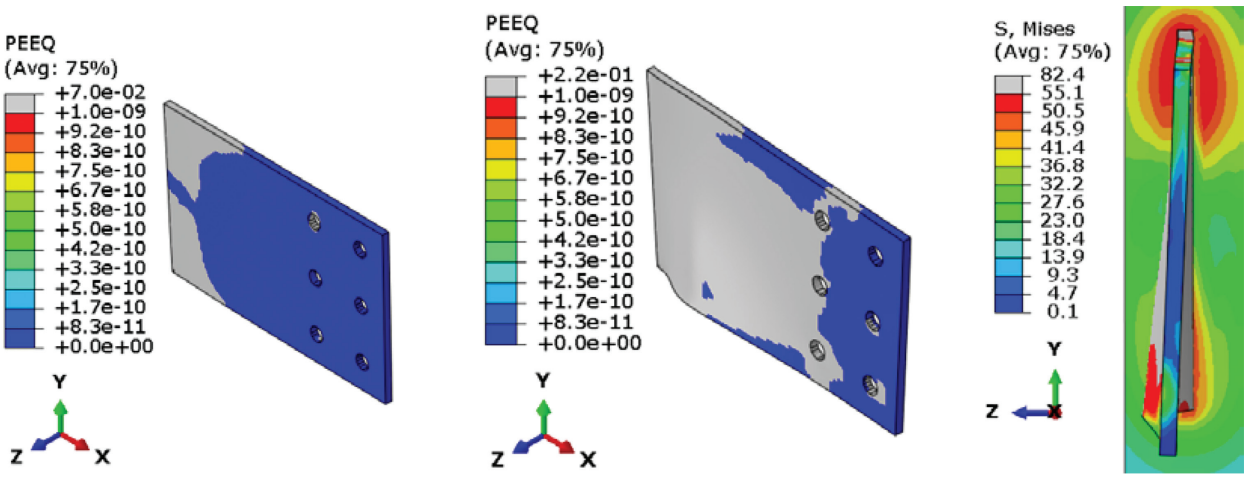

(a) Yielding at the gross section, Connection 4

(b) Yielding at net section, Connection 4

(c) Large out-of-plane deformation at the bottom of the plate, Connection 4

Fig. 7. Behavior of connections with W14×233 column.

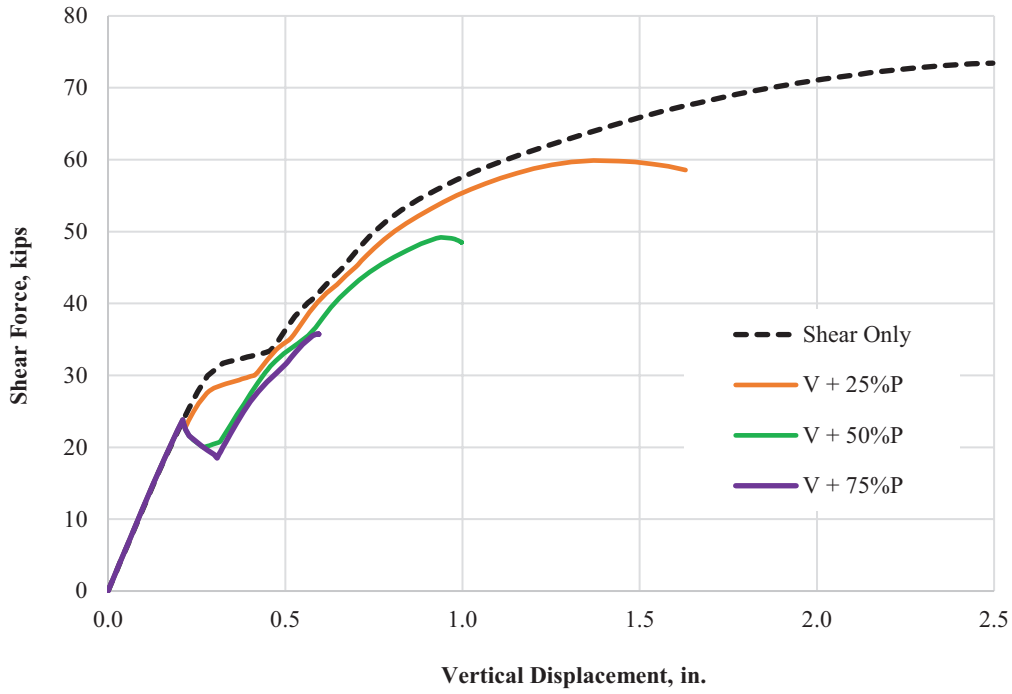

Fig. 8. Force-displacement plot for combined loading for Connection 1.

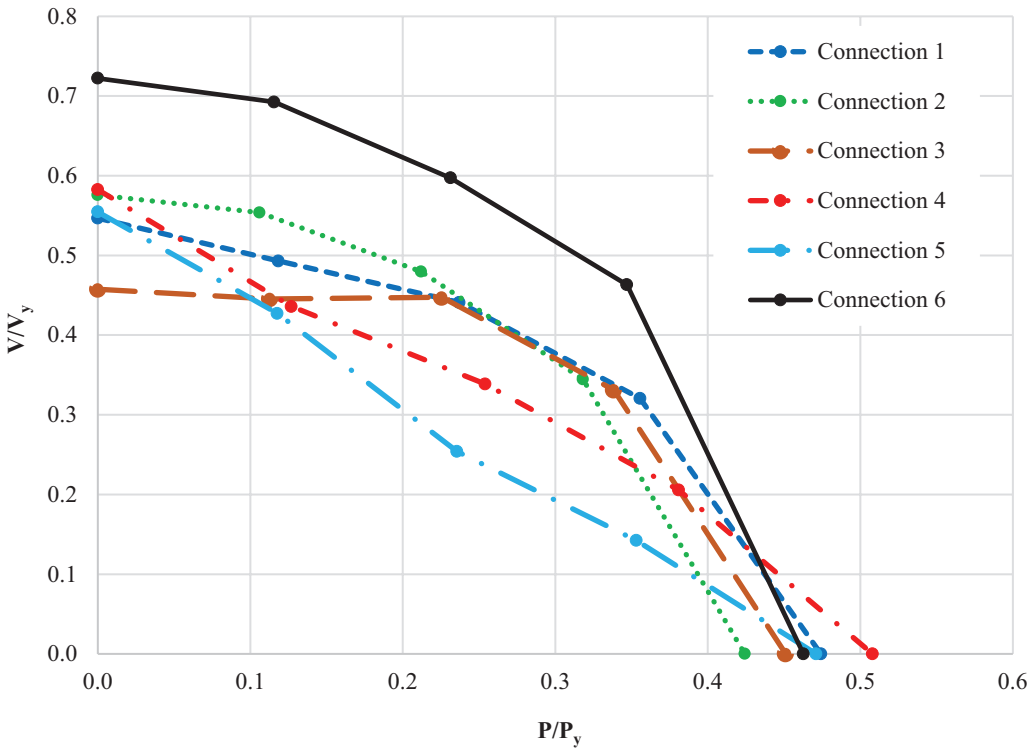

Fig. 9. Normalized shear-compression interaction plot (top flange continuously restrained case).

The comparison of the results from FE analysis with those of the different interaction equations discussed earlier is shown in Table 5. The ratio given in the table is the ratio of the strength obtained from FEA analysis to the results obtained by using the respective interaction equations. The design strength was used in the interaction equation for each term. The value of the resistance factor, ϕ, used for axial, flexural, and torsional strength, was 0.90, while 1.0 was applied for shear yielding strength. The AISC *Manual Companion* Example IIA-19B (2022b) was used to compute the required force and available strength. The flexural strength was determined using AISC *Specification* Section F11, where the limit state of flexural yielding governed for all connection configurations. To compute

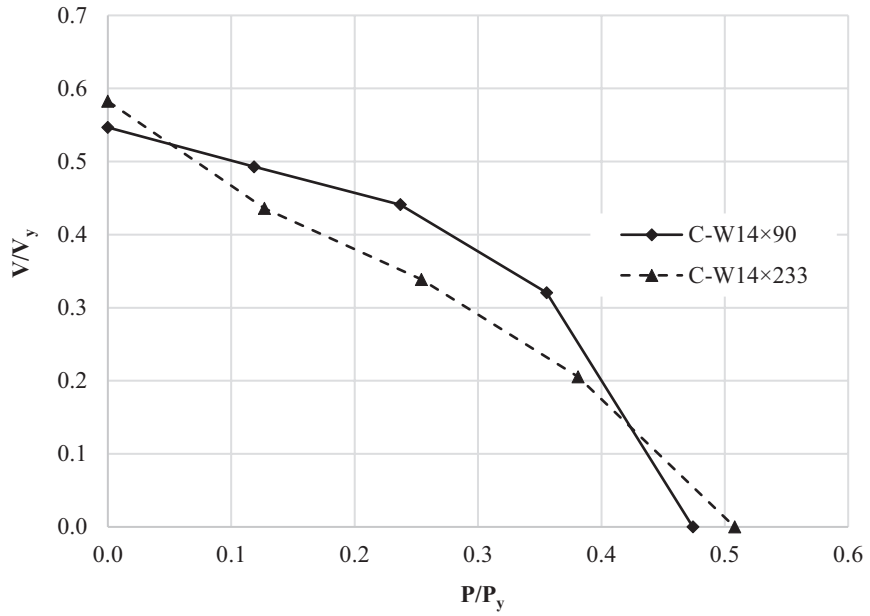

Fig. 10. Comparison of behavior of connection with a six-bolt configuration with W14×90 and W14×233 columns.

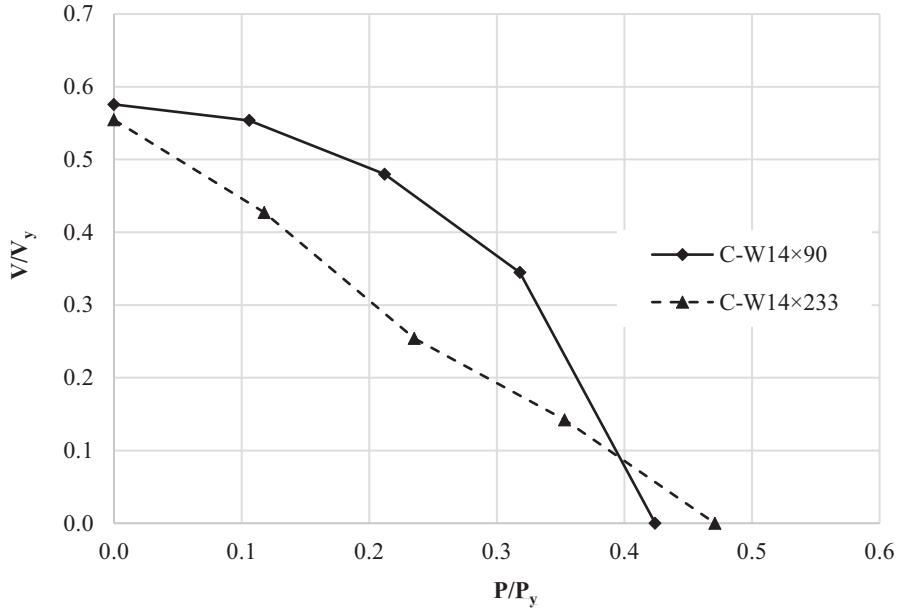

Fig. 11. Comparison of behavior of connection with an eight-bolt configuration with W14×90 and W14×233 columns.

Table 5. Comparison of Results with Interaction Equations for Top Flange Continuously Restrained							
				AISC *Manual* (2023) Eq. 9-1	Dowswell (2019)	AISC *Manual* (2023) Part 12	AISC *Manual* (2023) M_{ry} = 0 Case
	P/P_y	P, kips	V_{FEA}, kips	Ratio	Ratio	Ratio	Ratio
Connection 1	0.00	0.00	55.80	1.43	1.57	1.49	1.49
	0.12	22.04	55.00	1.57	1.87	4.57	1.91
	0.24	44.09	49.20	2.14	6.84	—	3.18
	0.36	66.13	35.78	12.78	—	—	23.20
	0.47	88.17	0.00	1.29	1.93	2.90	1.29
Connection 2	0.00	0.00	114.20	1.27	1.40	1.34	1.34
	0.11	35.06	109.85	1.26	1.53	2.35	1.42
	0.21	70.12	95.18	1.23	2.32	—	1.60
	0.32	105.18	68.36	1.12	—	—	1.65
	0.42	140.24	0.00	0.78	1.64	2.12	0.78
Connection 4	0.00	0.00	65.00	1.72	1.89	1.80	1.74
	0.13	23.62	48.64	1.46	1.76	5.15	1.75
	0.25	47.24	37.79	1.89	—	—	2.80
	0.38	70.85	22.93	—	—	—	—
	0.51	94.47	0.00	1.38	2.06	3.10	1.38
Connection 5	0.00	0.00	110.00	1.26	1.39	1.34	1.34
	0.12	38.93	84.73	1.02	1.30	2.13	1.17
	0.24	77.85	50.38	0.70	—	—	0.94
	0.35	116.78	28.20	0.54	—	—	0.82
	0.47	155.70	0.00	0.87	2.04	2.35	0.87
Connection 6	0.00	0.00	223.00	1.37	1.50	1.45	1.45
	0.12	59.75	214.62	1.35	2.06	2.75	1.52
	0.23	119.50	185.09	1.27	—	—	1.62
	0.35	179.25	143.55	1.18	—	—	1.68
	0.46	239.00	0.00	0.71	2.00	2.27	0.71

lateral-torsional buckling strength, the value of the bending modification factor, C_b was used as 1.84 (Dowswell, 2019). Similarly, the compressive strength of the plate was computed using AISC *Specification* Section J.4 (2016), with the effective length factor, k, set to 1.2. Because all the connection configurations had the ratio of effective length, L_c, to radius of gyration, r, greater than 25, AISC *Specification* Section E3 was applied. The strength was computed using the realistic material properties used in the analysis. It shows that AISC *Manual* Equations 12-2 and 12-3 (Equations 3 and 4) with a case of M_{ry} = 0 and AISC *Manual* Equation 9-1 (Equation 2) can safely predict the strength for a lower level of compression force. However, they can overpredict the strength for a higher level of compression force. Moreover, when the connection involves a larger column web stiffness, increased negative moment in the plate was observed due to the increased rigidity in the connection This resulted in a higher effect of the applied compression force on overall strength of the plate, causing FEA results to be lower than those predicted by the equations.

Since the equations were overpredicting strength for compression loading alone, it became apparent that equations incorporating out-of-plane moments were necessary. The AISC *Manual* interaction Equations 12-2 and 12-3 (Equations 5 and 6) were found to be excessively conservative when the weak-axis flexural term is included in the equation. Dowswell's (2019) equation (Equation 7) was slightly less conservative than the AISC *Manual* Equations 12-2 and 12-3 (Equations 5 and 6), but in some cases of combined loading, the results were still quite conservative.

Beam Bracing Case: Without Lateral Restraint on Top Flange

The failure mode for all connections when subjected to shear loading was twisting of the extended shear tab. The failure load for all connections is given in Table 6 on page 211. The force-displacement plot for shear loading and combined loading cases for Connection 1 is shown in Figure 12. The failure load was taken as the peak load in the force-displacement plot. The deformation in the plate and stress contour for connections 1 and 4 at the peak load is shown in Figure 13.

After analyzing the connection under shear load only, the connections were subsequently subjected to compression load and combined shear and compression forces. Once again, the connections were analyzed separately for three different cases: shear load plus compression force equal to 25%, 50%, and 75% of the total compressive strength obtained from the analysis. The application of compression force resulted in a decrease in the shear strength of the plate, with a greater effect observed at a higher level of compression force. A shear-compression interaction plot was generated, which was normalized against the shear yield strength

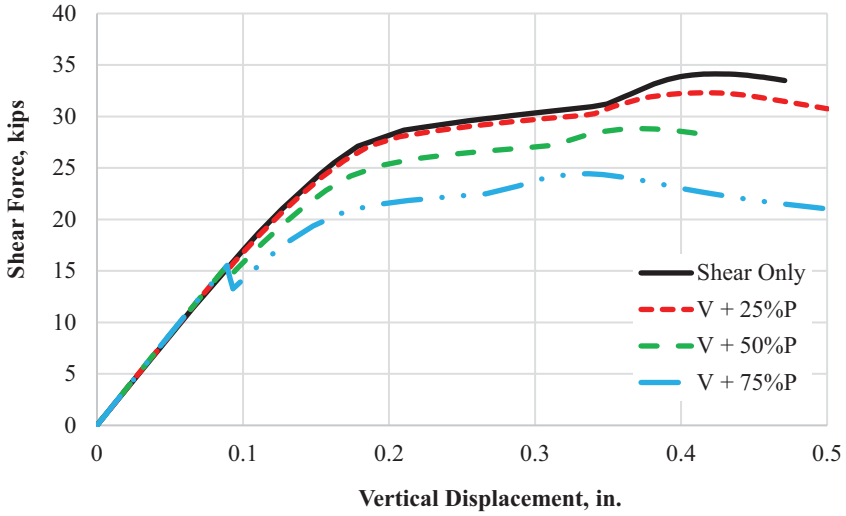

Fig. 12. Force-displacement plot for combined loading for Connection 1.

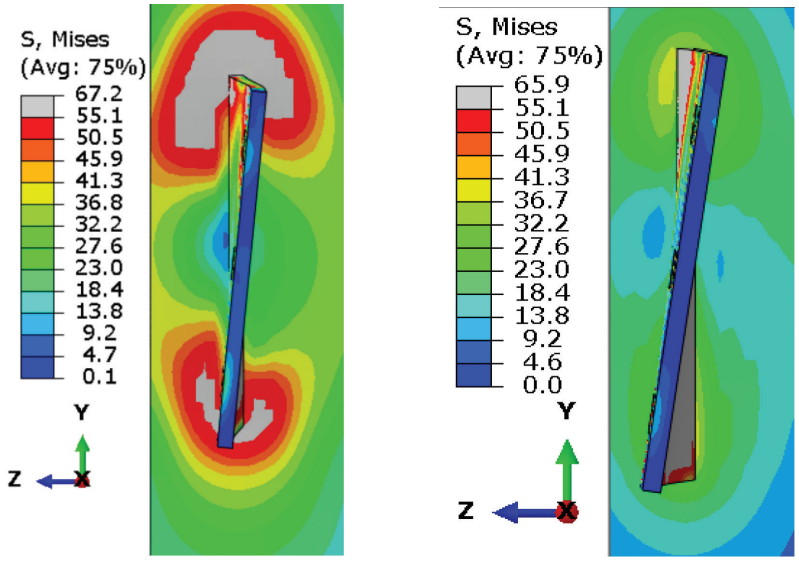

(a) Connection 1 *(b) Connection 4*

Fig. 13. Stress contour plot showing deformation of the plate at peak load.

and axial yield strength of the plate. This plot is presented in Figure 14 for all the connections. The obtained ratio of shear strength to nominal shear yield strength ranged from 0.31 to 0.45, while the obtained ratio of compressive strength to nominal axial yield strength ranged from 0.23 to 0.32.

All three connection configurations were analyzed with the W14×90 column and the W14×233 column. The comparison of interaction plots for two different column sizes is shown in Figures 15, 16, and 17. The figures show that at a lower level of the compression force, the effect of compression force on shear strength is similar for both column sizes. However, at a higher level of compression force, the effect is more pronounced for the flexible column (W14×90).

The comparison of results from the FE analysis with different interaction equations discussed earlier is presented in Table 6. The table shows that the equations that do not include the out-of-plane moment (Equations 2, 3, and 4) consistently overpredict the strength, while Dowswell's (2019) equation (Equation 7) can predict the strength with good accuracy. However, there are some cases where the ratio of observed strength-to-predicted strength is less than 1 by a few percentage points.

Beam Bracing Case: Single Point Restraint Near the Connection

Adding a single point lateral restraint near the connection end prevented the early failure of the connection due to twisting of the plate. The behavior under shear loading was similar to the case of beam bracing, where the top flange was continuously restrained in the lateral direction. The force-displacement plot for shear loading and combined loading cases for Connection 1 is shown in Figure 18. Similarly, Connection 3 failed due to shear failure of the bolt, just like in the beam bracing case with continuous restraint of the top flange.

The application of a compression force results in a decrease in the shear strength of the plate, with the extent of the effect depending on the column size used. A shear-compression interaction plot, normalized against the shear yield strength and axial yield strength of the plate, was generated. This plot is presented in Figure 19 for all connections. The obtained ratio of shear strength to nominal shear yield strength ranged from 0.44 to 0.65, while the obtained ratio of compressive strength to nominal axial yield strength ranged from 0.32 to 0.43.

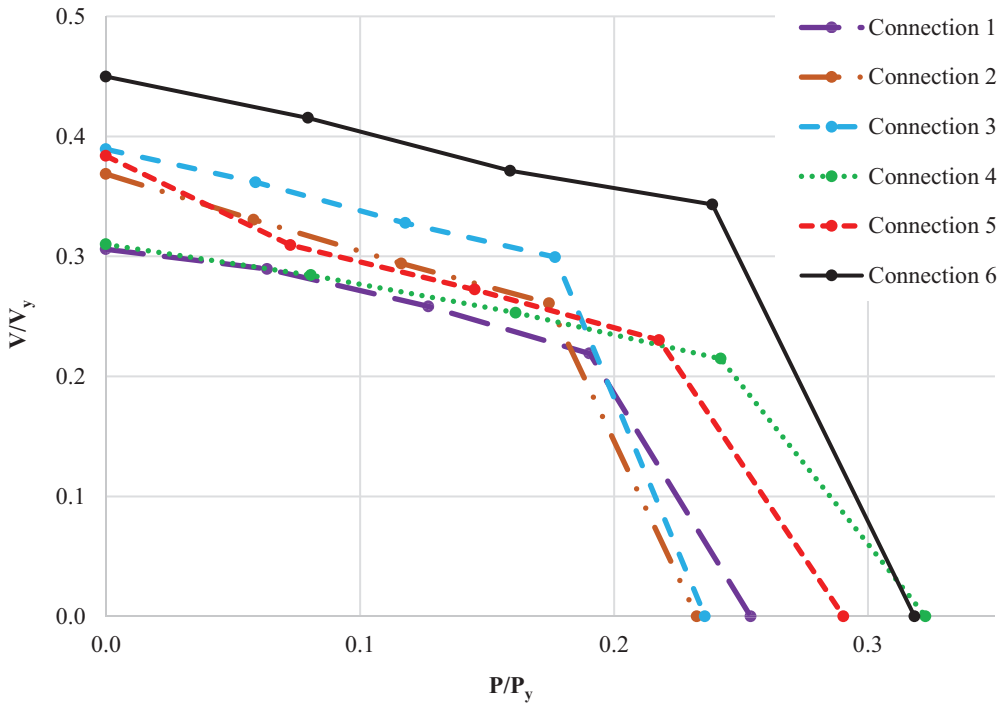

Fig. 14. Normalized shear-compression interaction plot (beam bracing case: without lateral restraint on top flange).

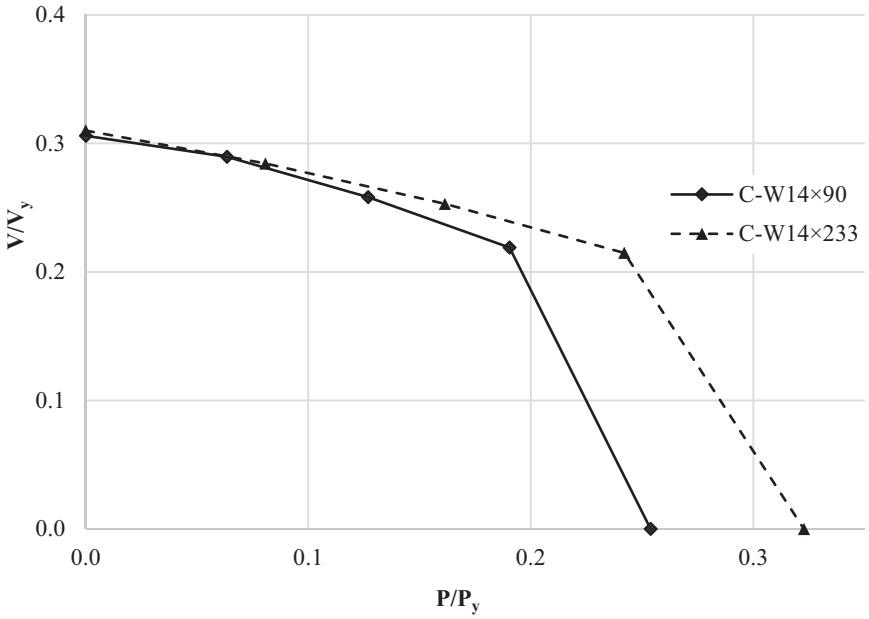

Fig. 15. Comparison of behavior of connection with a six-bolt configuration with W14×90 and W14×233 columns.

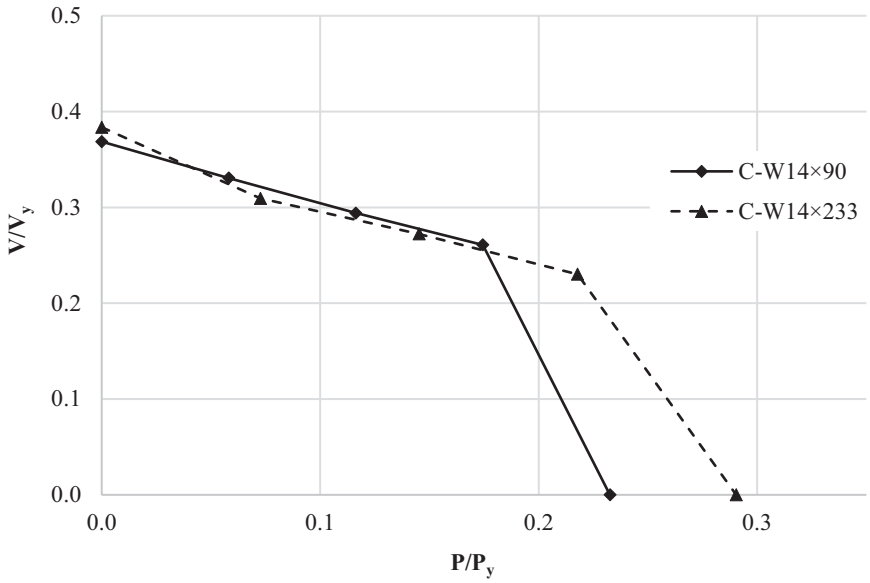

Fig. 16. Comparison of behavior of connection with an eight-bolt configuration with W14×90 and W14×233 columns.

The comparison of interaction plots for two different column sizes is shown in Figures 20 and 21. It was found that the effect of the column size on the behavior of the extended shear tabs under combined loading of shear and compression in this beam bracing case is similar to the beam bracing case where the top flange is continuously braced in the lateral direction. The results show that, at lower levels of compression force, the rate of decrease in shear strength is greater for a rigid support compared to a flexible support. However, at higher levels of compression force, the effect of the compression force was more evident for a flexible support.

The comparison of results from the FE analyses with different interaction equations discussed earlier is shown in Table 7. The observations for a single point restraint in the top flange near the connection end are similar to the case of continuous restraint.

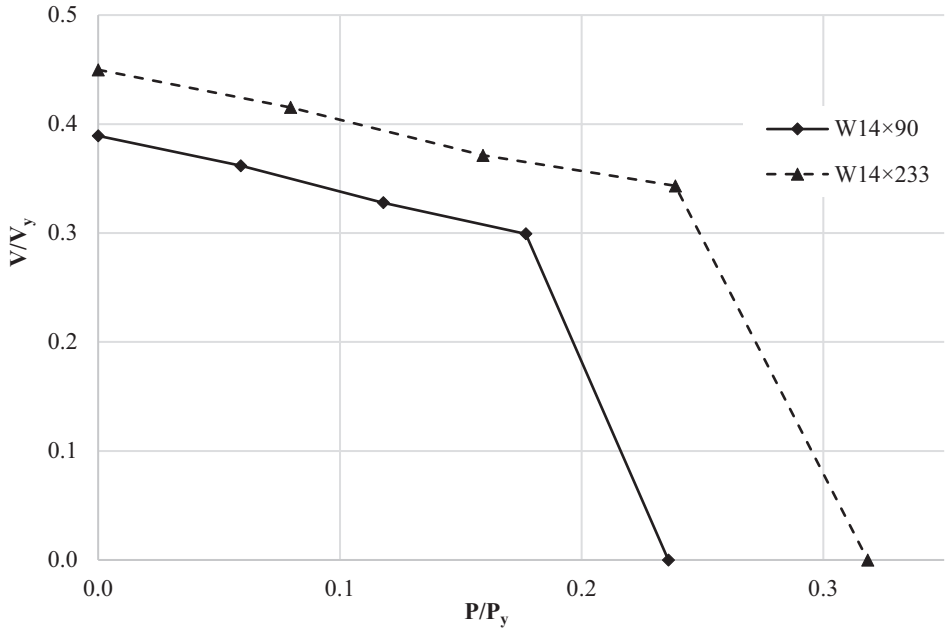

Fig. 17. Comparison of behavior of connection with a 10-bolt configuration with W14×90 and W14×233 columns.

Table 6. Comparison of Results with Interaction Equations for No Restraint on Top Flange							
				AISC *Manual* (2023) Eq. 9-1	Dowswell (2019)	AISC *Manual* (2023) Part 12	AISC *Manual* (2023) $M_{ry} = 0$ Case
	P/P_y	P, kips	V_{FEA}	Ratio	Ratio	Ratio	Ratio
Connection 1	0.00	0.0	34.1	0.87	1.07	0.91	0.91
	0.06	11.8	32.3	0.85	1.10	1.26	0.94
	0.13	23.6	28.8	0.83	1.29	2.93	1.04
	0.19	35.4	24.4	0.85	10.81	—	1.18
	0.25	35.6	47.2	0.69	1.33	1.55	0.69
Connection 2	0.00	0.0	73.1	0.81	1.01	0.86	0.86
	0.06	19.2	65.6	0.74	0.96	1.02	0.81
	0.12	38.5	58.3	0.68	0.98	1.39	0.78
	0.17	57.7	51.8	0.63	1.20	3.89	0.79
	0.23	76.3	76.9	0.43	1.01	1.16	0.43
Connection 3	0.00	0.0	120.6	0.72	0.94	0.76	0.76
	0.06	30.5	112.1	0.67	0.92	0.93	0.74
	0.12	60.9	101.6	0.62	0.96	1.29	0.70
	0.18	91.4	92.8	0.59	1.23	3.47	0.71
	0.24	119.4	121.8	0.36	1.02	1.16	0.36
Connection 4	0.00	0.0	34.6	0.92	1.11	0.96	0.96
	0.08	15.0	31.7	0.88	1.11	1.51	1.00
	0.16	30.0	28.2	0.92	1.31	47.86	1.22
	0.24	45.1	24.0	1.11	5.79	—	1.67
	0.25	45.7	60.1	0.88	1.31	1.98	0.88
Connection 5	0.00	0.0	76.1	0.87	1.08	0.92	0.92
	0.07	24.0	61.4	0.72	0.94	1.07	0.79
	0.15	48.0	54.0	0.66	1.05	2.00	0.79
	0.22	72.0	45.7	0.62	2.36	—	0.80
	0.29	76.3	96.0	0.53	1.26	1.45	0.53
Connection 6	0.00	0.0	139.4	0.86	1.11	0.91	0.91
	0.08	41.1	128.7	0.80	1.53	1.25	0.89
	0.16	82.2	115.1	0.74	1.87	2.74	0.88
	0.24	123.3	106.4	0.74	4.48	—	0.95
	0.32	119.4	164.5	0.73	1.38	1.56	0.49

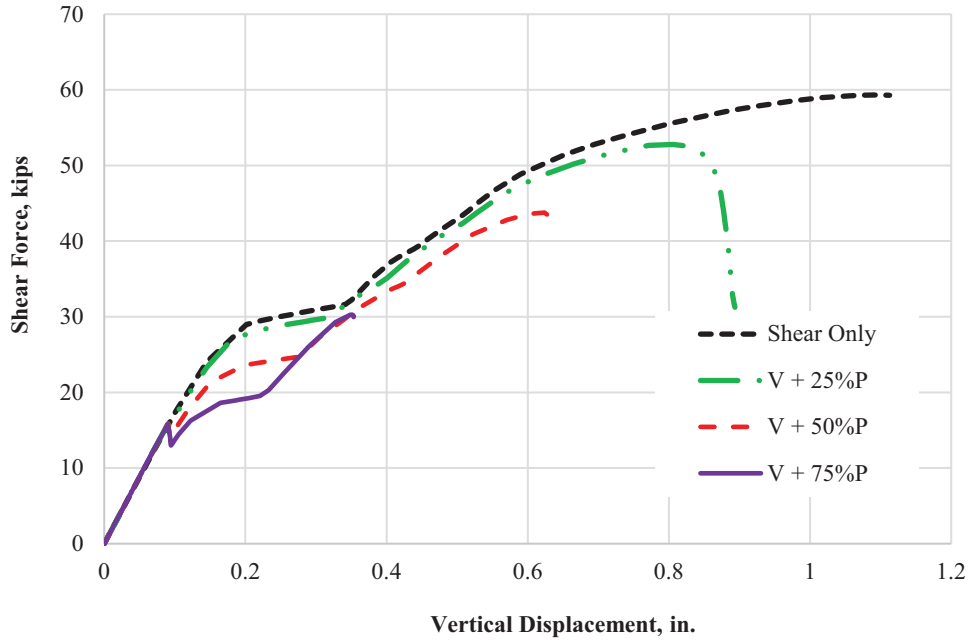

Fig. 18. Force-displacement plot for combined loading for Connection 1.

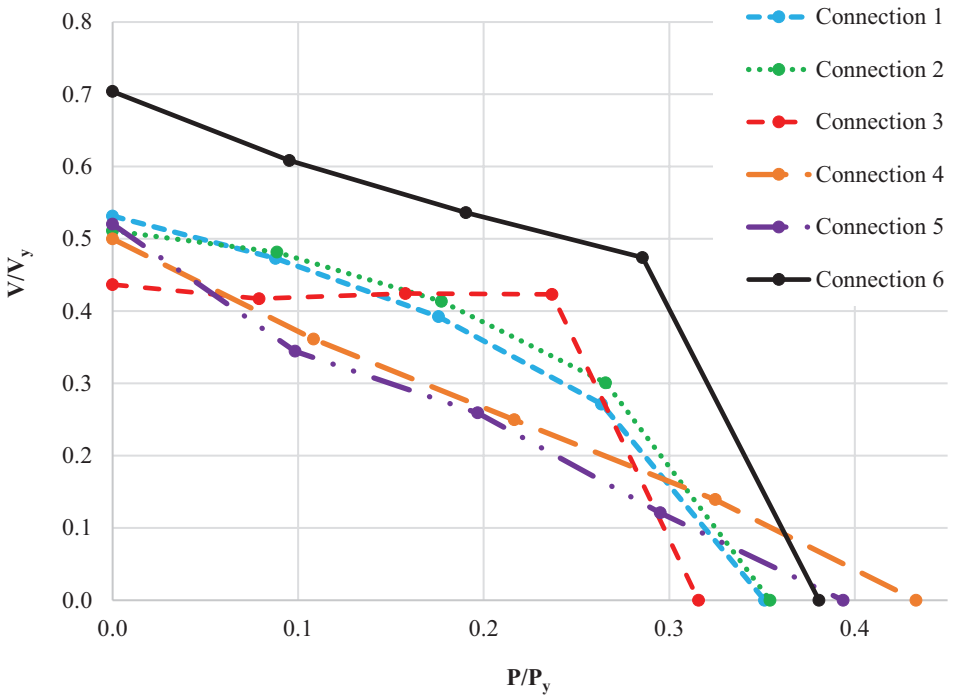

Fig. 19. Normalized shear-compression interaction plot (beam bracing case: single point restraint in top flange near the connection).

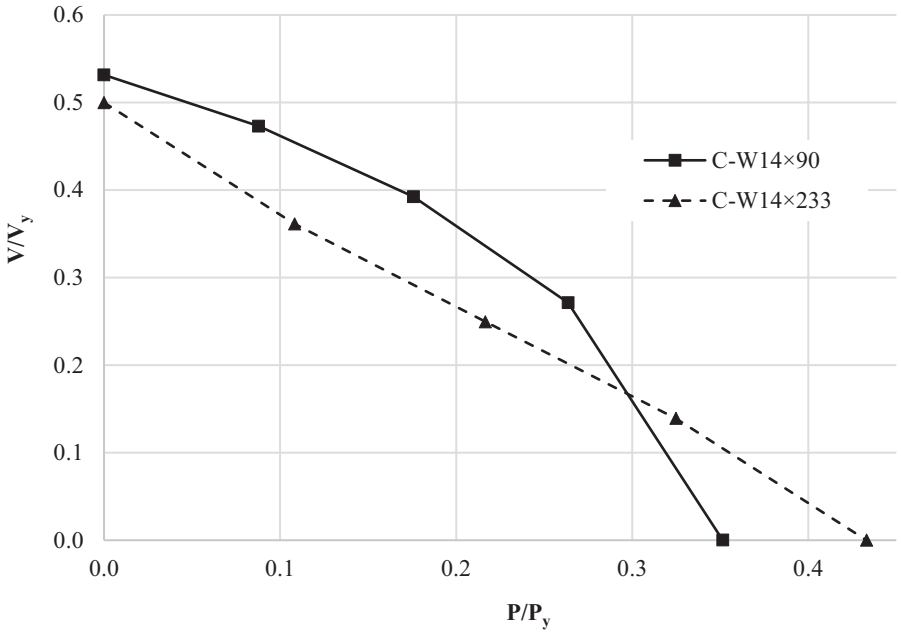

Fig. 20. Comparison of behavior of connection with a six-bolt configuration with W14×90 and W14×233 columns.

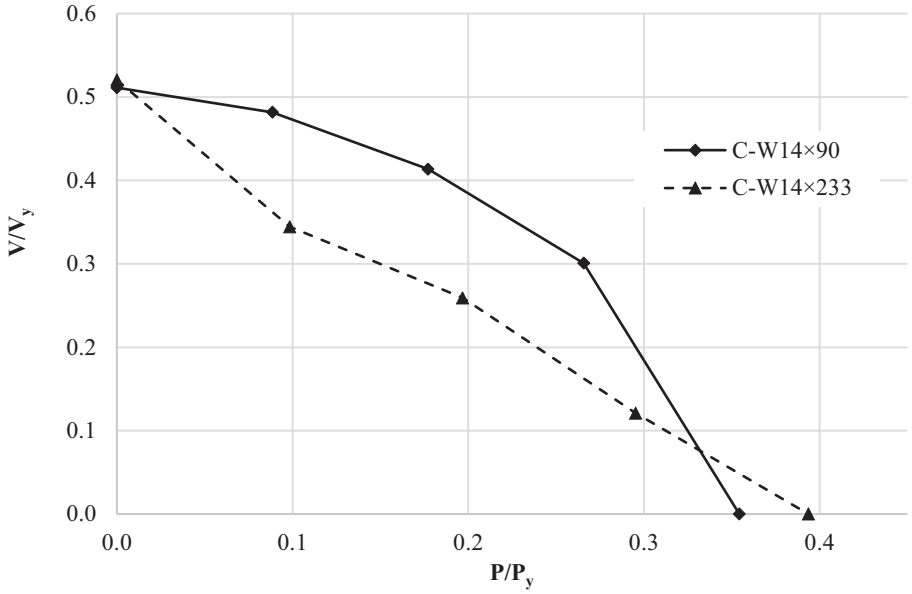

Fig. 21. Comparison of behavior of connection with an eight-bolt configuration with W14×90 and W14×233 columns.

Table 7. Comparison of Results with Interaction Equations for Single Point Restraint on Top Flange Near the Connection							
	P/P_y	P, kips	V_{FEA}	AISC *Manual* (2023) Eq. 9-1	Dowswell (2019)	AISC *Manual* (2023) Part 12	AISC *Manual* (2023) $M_{ry} = 0$ Case
				Ratio	Ratio	Ratio	Ratio
Connection 1	0.00	0.00	59.3	1.52	1.85	1.59	1.59
	0.24	16.33	52.8	1.43	1.93	2.65	1.65
	0.48	32.67	43.8	1.44	4.08	—	1.95
	0.72	49.00	30.3	1.57	—	—	2.44
	0.52	65.33	0.0	0.95	1.84	2.15	0.95
Connection 2	0.00	0.00	101.4	1.13	1.41	1.19	1.19
	0.09	29.28	95.5	1.09	1.48	1.79	1.21
	0.18	58.57	82.0	1.01	1.94	6.87	1.25
	0.27	87.85	59.6	0.85	—	—	1.18
	0.35	117.13	0.0	0.65	1.54	1.77	0.65
Connection 4	0.00	0.00	55.8	1.48	1.62	1.55	1.55
	0.11	20.13	40.3	1.17	1.37	2.84	1.40
	0.22	40.26	27.8	1.12	2.04	—	1.62
	0.32	60.39	15.5	1.83	—	—	3.09
	0.25	80.53	0.0	1.18	1.76	2.65	1.18
Connection 5	0.00	0.00	103.2	1.19	1.47	1.25	1.25
	0.18	32.54	68.3	0.81	1.11	1.43	0.91
	0.36	65.07	51.4	0.67	1.58	30.51	0.85
	0.54	97.61	24.0	0.38	1.20	—	0.55
	0.42	130.14	0.0	0.72	1.70	1.97	0.72
Connection 6	0.00	0.00	218.1	1.34	1.73	1.42	1.42
	0.15	49.17	188.6	1.18	2.33	2.05	1.31
	0.29	98.33	166.2	1.10	3.55	12.52	1.34
	0.44	147.50	147.0	1.08	—	—	1.46
	0.35	196.67	0.0	0.88	1.65	1.87	0.58

Note: Connection 3 results are not reported due to the predicted failure by bolt fracture.

CONCLUSIONS

The major goal of this research was to investigate the behavior of extended shear tab connections when subjected to combined loading of shear and compression forces and to validate the use of available interaction equations. To achieve this goal, 18 finite element models of extended shear tabs with different practical connection configurations were developed and analyzed in ABAQUS for the case of combined loading. The effect of a compression force on the shear strength was studied by analyzing the force-displacement plot, stress contour, deformed shape, and generated shear-compression interaction plot. The results from the analysis were compared with the available interaction equations in the AISC *Manual*, AISC *Specification*, and literature. Based on the research, the following conclusions can be derived:

1. **Effect of the bracing condition of the beam:** The beam bracing condition affects the shear strength and failure mode of the extended shear tabs, be it for shear loading alone or for the combined loading of shear and compression force. The shear strength when no form of bracing is provided in the beam top flange is significantly lower, and connections fail by twisting of the plate. The addition of a single point restraint near the

connection prevents the early twisting failure of the shear tab, and thus significantly improves the shear strength. When the top flange of the beam is continuously braced, the failure mode observed was yielding of the cross section in all cases but one, which failed by bolt fracture.

Use of the interaction equations: Because the shear strength and failure mode of the extended shear tabs depend on the beam bracing condition, different interaction equations are found to be effective for different bracing conditions of the beam. When the top flange of the beam is continuously restrained, equations that do not include the out-of-plane moment terms (AISC *Manual* Equation 9-1, Equations 12-2 and 12-3 with case $M_{ry} = 0$) shown as Equations 2, 3, and 4 herein, can safely predict the strength for a lower level of compression force. However, it can overpredict the strength for a higher level of compression force. Moreover, when the connection involves a column with larger web stiffness, an increased negative moment was observed that resulted in a higher effect of the applied compression force on the shear strength of the plate, causing FEA results to be lower than those predicted by the equations. Since the equation was overpredicting results for compression loading alone, it became apparent that equations incorporating out-of-plane moments were necessary. The equations provided in AISC *Manual* Part 12 that include the weak-axis flexural term (Equations 5 and 6) were found to be overly conservative for this case. Dowswell's (2019) equation (Equation 7) was less conservative than those equations, but in some cases of combined loading, the results were still overly conservative.

When no bracing is provided in the beam top flange, equations that do not include the out-of-plane moments overpredict the strength. In these situations, Dowswell's (2019) equation (Equation 7) can predict the strength with good accuracy.

The conclusions for single point restraint in the top flange near the connection end are similar to those for the continuously restrained case.

2. **Effect of the support condition:** For a top flange that is continuously braced or is braced at a single point near the connection, the effect of a compression force on the shear strength is more significant in the case of a rigid support at a lower level of compression force. As the level of compression force becomes higher, its effect will be higher for a flexible support.

   For a beam unbraced on the top flange, the support condition does not have an influence on the effect of compression force on shear strength for lower levels of compression force. However, for higher levels of compression force, the effect is more evident for flexible columns.

Therefore, while designing, it would be more reliable to use the equation proposed by Dowswell (2019) (Equation 7) to compute the strength safely. Because the results from this equation are much more conservative for cases where continuous or single-point restraint is provided in the top flange, the required weak-axis moment in the equation for these two cases can be decreased to a certain percentage of the value that would have been obtained by using a geometric eccentricity. In this case, decreasing the weak-axis eccentricity to 60% of the geometric eccentricity still yielded an actual-to-predicted strength ratio greater than 1.

SYMBOLS

C_b Bending modification factor

M_c Available plastic moment strength of the plate (kip-in.)

M_{cx} Available strong-axis plastic moment strength of the plate (kip-in.)

M_{cy} Available weak-axis plastic moment strength of the plate (kip-in.)

$M_r = M_u$ Required (ultimate) moment strength of the plate (kip-in.)

$M_{rx} = V_u a$ Required strong-axis moment strength of the plate (kip-in.)

$M_{ry} = P_r\left(\frac{t_p + t_w}{2}\right)$ Required weak-axis moment strength of the plate (kip-in.)

P_c Available axial strength of the plate (kips)

P_r Required axial strength of the plate (kips)

T_c Available torsional strength (kip-in.)

T_r Required torsional strength $= V_r\left(\frac{t_p + t_w}{2}\right)$ (kip-in.)

$V_c = \phi_v V_n$ Available shear yielding strength of the plate (kips)

$V_r = V_u$ Required (ultimate) shear strength (kips)

a Distance from the face of the support to the first vertical line of bolts, in.

d_b Depth of beam, in.

l_{ev} Vertical edge distance, in.

l_{eh} Horizontal edge distance, in.

t_p Thickness of the plate, in.

t_w Thickness of the beam web (in.)

REFERENCES

ABAQUS (2022), *ABAQUS/CAE User's* Guide, Dassault Systemes Simulia Corporation, Waltham, Mass.

AISC (2016), *Specification for Structural Steel Buildings,* ANSI/AISC 360-16*,* American Institute of Steel Construction, Chicago, Ill.

AISC (2017), *Steel Construction Manual,* 15th Ed., American Institute of Steel Construction, Chicago, Ill.

AISC (2022a), *Specification for Structural Steel Buildings,* ANSI/AISC 360-22*,* American Institute of Steel Construction, Chicago, Ill.

AISC (2022b), *Companion to the AISC Steel Construction Manual—Volume 1: Design Examples,* American Institute of Steel Construction, Chicago, Ill.

AISC (2023), *Steel Construction Manual,* 16th Ed., American Institute of Steel Construction, Chicago, Ill.

Asl, M.H., Farivar, B., and Momenzadeh, S. (2019), "Investigation of the Rigidity of Welded Shear Tab Connections," *Engineering Structures*, Vol. 179, pp. 353–366.

ASTM (2021), *Standard Specification for High-Strength Low-Alloy Columbium-Vanadium Structural Steel*, ASTM A572/572M-21e1, ASTM International, West Conshohocken, Pa.

ASTM (2022), *Standard Specification for Structural Steel Shapes*, ASTM A992/A992M, ASTM International, West Conshohocken, Pa.

ASTM (2023), *Standard Specification for High Strength Structural Bolts and Assemblies, Steel and Alloy Steel, Heat Treated, In. Dimensions 120 ksi and 150 ksi Minimum Tensile Strength, and Metric Dimensions 830 MPa and 1040 MPa Minimum Tensile Strength*, ASTM F3125/F3125M, ASTM International, West Conshohocken, Pa.

Dowswell, B. (2016), "A Notional Load Yield Line Model for Gusset Plate Stability," *Proceedings of the AISC North American Steel Construction Conference*, April 13–15, Orlando, Fla.

Dowswell, B. (2019), "Torsion of Rectangular Connection Elements," *Engineering Journal*, AISC, Vol. 56, No. 2, pp. 63–87.

Ganaganur Anantharam, V.A. (2022), "Finite Element Analysis of Stabilizer Plates in Single Plate Shear Connection Using ABAQUS," Master's Thesis, University of Cincinnati, Cincinnati, Ohio.

Mirzaei, A. (2014), "Steel Shear Tab Connections Subjected to Combined Shear and Axial Forces," PhD Dissertation, McGill University, Montreal, Quebec, Canada.

Muir, L.S. and Hewitt, C.M. (2009), "Design of Unstiffened Extended Single-Plate Shear Connections," *Engineering Journal*, AISC, Vol. 46, No. 2, pp. 67–79.

Nasrabadi, M.M. (2018), *Behaviour of Extended Shear Tab Connections under Combined Axial and Shear Forces,* PhD Thesis, McGill University, Montreal, Quebec.

Rahman, A., Mahamid, M., Amro, A., and Ghorbanpoor, A. (2007), "The Analyses of Extended Shear Tab Steel Connections Part I: The Unstiffened Connections," *Engineering Journal*, AISC, Vol. 44, No. 2, pp. 117–132.

Ruffley, D.J. (2011), "A Finite Element Approach for Modeling Bolted Top-and-Seat Angle Components and Moment Connections," Master's Thesis, University of Cincinnati, Cincinnati, Ohio.

Salem, P. (2016), "Unified Design Criteria for Steel Cantilever Plate Connection Elements," PhD Thesis, University of Alberta, Edmonton, Alberta, Canada.

Thomas, K. (2014), "Design and Behaviour of Extended Shear Tabs under Combined Loads," Master's Thesis, University of Alberta, Edmonton, Alberta, Canada.

Steel Structures Research Update

Seismic Local Buckling Limits for Hollow Structural Section and Built-Up Box Columns

JUDY LIU

INTRODUCTION

Recently completed research on seismic local buckling limits for steel hollow structural section (HSS) and built-up box columns is featured. These National Center for Research on Earthquake Engineering (NCREE) studies are led by Dr. Chung-Che Chou and Dr. Tung-Yu Wu in the Department of Civil Engineering at National Taiwan University (NTU). Dr. Chou also serves as the NCREE Director. Dr. Chou's research has focused on seismic testing, analysis, and design for steel and post-tensioned self-centering structures. Some recent work includes studies on hybrid simulation of a full-scale steel moment frame, a post-tensioned self-centering brace, novel prediction models for early earthquake warnings, and earthquake reconnaissance work in eastern Taiwan. Dr. Chou's numerous accolades include the Awards for Excellent Research and Technology Transfers for his leadership on a research team developing a sandwiched buckling-restrained brace and a self-centering brace. Dr. Wu's research interests include collapse behavior of cold-formed HSS columns under seismic loading, subwavelength seismic metamaterial structures, crack growth in railway crossings under high wheel-rail impacts, and seismic resilience of steel buildings. In addition to multiple scholarships and fellowships, Dr. Wu's honors include the Raymond C. Reese Research Prize, awarded by the American Society of Civil Engineers (ASCE) for papers representing notable achievements in research with impact on design. The National Science and Technology Council is supporting this research on seismic local buckling limits for HSS and built-up box columns. Selected highlights from both projects are presented, along with a preview of future research tasks.

BACKGROUND AND OBJECTIVES

Seismic local buckling limits for HSS and built-up box columns have garnered interest due to some inconsistencies and conservatism. The seismic local buckling limits for HSS, for example, are quite different across seismic design codes in the United States, Japan, and Taiwan. The discrepancies are partially attributed to inconsistent loading protocols used in HSS research (Teng et al., 2023). Limits for HSS and built-up box columns have also been shown to be conservative (Lin and Chou, 2022; Teng et al., 2023). Through the featured research, complemented by concurrent studies led by Dr. Jason McCormick (University of Michigan) and Dr. Chia-Ming Uang (University of California–San Diego), Drs. Chou and Wu have been working to resolve these issues.

Research teams led by Drs. Chou and Wu aim to improve efficiency in HSS and built-up box column design through integrated experimental and computational studies focused on their seismic local buckling limits. Specific objectives for HSS and built-up box columns are to:

1. Characterize their seismic performance under combined axial and cyclic lateral loadings.
2. Extend the seismic performance knowledge base through a computational parametric study.
3. Evaluate the level of conservatism of the compactness requirements in existing seismic design provisions.
4. Propose highly and moderately ductile width-thickness limits.

HSS COLUMNS

A coordinated experimental-numerical investigation has provided insights into the seismic behavior of HSS columns. The experimental work demonstrated seismic performance relative to axial loading, element and member slenderness. Finite element simulations extended the work and aided in defining critical story-drift angles for the box columns. Revised seismic local buckling limits have been proposed based on this research.

Test Specimens, Test Setup, and Loading Protocol

Parameters investigated for six half-scale HSS columns included cross-section sizes, element width-to-thickness ratios, member slenderness, and grade of steel. The square HSS ranged from nominal 4 in. to 8 in. sections. Width and height dimensions, B and H, were 3.94 in., 5.91 in., 6.89 in.,

Judy Liu, PhD, Research Editor of the AISC *Engineering Journal*, Professor, Oregon State University, School of Civil and Construction Engineering, Corvallis, Ore. Email: judy.liu@oregonstate.edu\

and 7.87 in. Thickness, t, ranged from 0.236 in. to 0.472 in. For element slenderness, following the AISC *Specification* (2022a), 3 times the thickness, t, was subtracted from B and H to obtain b and h, the flat widths across each side. The resulting b/t and h/t values were 8.9, 14.9, 23.9, and 26.2. The element width-to-thickness ratio of 14.9 was evaluated for three nominal B and H values, allowing comparison for three different member slenderness values (i.e., length divided by radius of gyration, L/r). The ratio of 8.9 satisfies λ_{hd}, the width-to-thickness limit for a highly ductile member, while 14.9 satisfies λ_{md}, the limit for a moderately ductile member (AISC, 2022b). Most specimens were fabricated using steel grade STKR 490 with a specified minimum yield stress of 47.1 ksi. Similar to A500 grades, STKR490 HSS may be cold-formed from flat steel plate and welded. A design thickness of 0.93 times the nominal thickness was used in the b/t calculations. One specimen, with element width-to-thickness ratio of 26.2, used BCR 295 for tubes that were cold-formed from welded steel pipes, with a specified minimum yield stress of 42.8 ksi. The nominal thickness was used in the b/t calculations for BCR 295.

The specimens were subjected to axial compression and cyclic lateral loading. The Multi-Axial Testing System (MATS) shown in Figure 1 imposed fixed-fixed boundary conditions. For each specimen, a constant axial force, P, equal to 0.2 times the nominal axial yield force, P_y, was applied. The axial force was also reported in terms of P_{ya}, the yield strength calculated using the measured, or actual yield stress. The axial loading for these specimens ranged from 0.13 to 0.16 of P_{ya}. The cyclic lateral loading protocol of increasing displacements corresponding to increasing story-drift angles (e.g., 0.01, 0.02, 0.03 rad…) followed AISC *Seismic Provisions* Section K2 (AISC, 2022b).

Experimental Results

The test specimens exhibited overall similar behavior with differences in the hysteretic response. Local buckling was observed at the ends of the columns. The buckled shapes were either (1) outward at opposite sides and inward at the other opposite sides (Figure 2), or (2) outward at four sides. Figure 2 shows the first type of buckled shape for an STKR 490 specimen with $b/t = 23.9$ and $P/P_{ya} = 0.15$ in the second cycle of the 0.06 rad. A sample moment versus story-drift angle response is shown in Figure 3. The moment, M, has been normalized by the plastic moment capacity, M_{pc}, of the column. The results are for a nominal $6 \times 6 \times 0.25$ in.

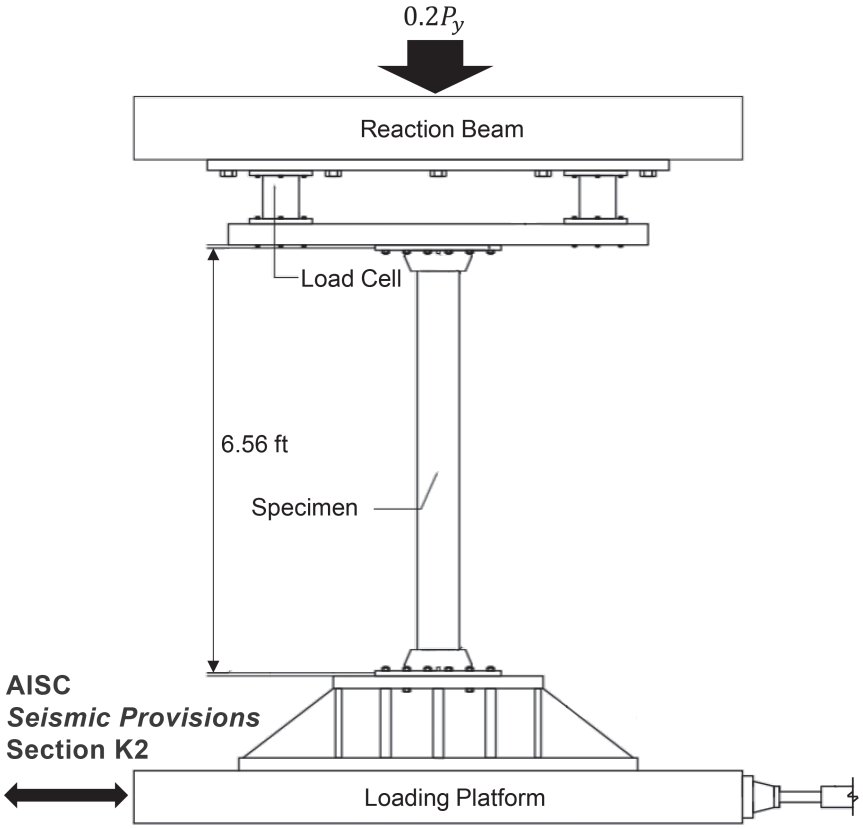

Fig. 1. Multi-Axial Testing System (MATS), shown here with HSS column specimen.

column with $b/t = 23.9$, $L/r = 34.2$, and $P/P_{ya} = 0.15$. Dashed lines in Figure 3 show the critical story-drift angle, SDA_{cr}, defined as the average of the story-drift angles (SDAs) corresponding to the positive and negative peak moment strength. The specimen has a $b/t = 23.9$ larger than $\lambda_{md} = 21.0$ but has an $SDA_{cr} = 0.03$; this is larger than expected ductility of 0.02 rad for a moderately ductile member. The tested specimens consistently exhibited better ductility than expected (e.g., 0.04 rad for a highly ductile member). The SDA_{cr} values ranged from 0.02 rad for a specimen with $b/t = 26.2$ to 0.09 for $b/t = 8.9$. The rest of the SDA_{cr} values were 0.03, 0.04, or 0.05. These results motivated the numerical investigation to follow.

Finite Element Simulation

Finite element simulations complemented the experimental test program. The finite element modeling approach corresponded to the experimental test setup and cyclic behavior of the HSS columns. Fully integrated shell elements and a nonlinear material model with kinematic hardening were used with the explicit solver in LS-DYNA (2013). Global and local geometric imperfections of $L/1500$ and $B/200$ were imposed (Figure 4). The columns were fully fixed at the bottom and fixed at the top except for lateral and vertical displacements.

The parameters for the computational study extended the experimental test program. An extensive analysis matrix included 33 sections of BCR 295 steel and 64 sections of BCP 325 steel. BCR 295 uses the cold-roll-forming process, and BCP 325 uses a cold-press process (Takeshi and Takuya, 2020). Each column was analyzed for three different P/P_y ratios (0.2, 0.3, 0.4), totaling 291 numerical simulations.

The numerical simulation results were used to extend the experimental test program and explore alternative seismic local buckling limits. The column results were plotted with respect to b/t and P/P_{ya} (Figure 5). Figure 5, with results for BCR 295 steel, shows how the SDA_{cr} changes with b/t and P/P_{ya}. The results are also compared to current moderately ductile, λ_{hd}, and highly ductile, λ_{hd}, limits, shown with dashed lines. Multivariate regression analysis was used to develop an SDA_{cr} equation with input parameters b/t, P/P_{ya}, and F_{ya}/E, where F_{ya} is the yield stress and E is the elastic modulus. The results were also modified for the effects of boundary conditions and loading protocol, following the

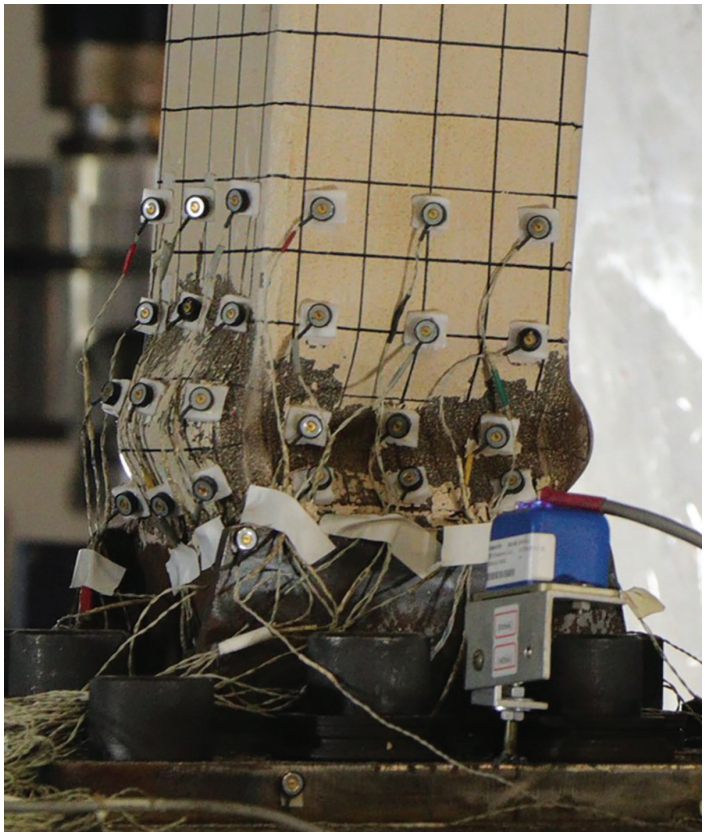

Fig. 2. Common failure mode of HSS columns—inward flange buckling and outward web buckling (photo is for a test specimen with $b/t = 23.9$, $P/P_{ya} = 0.15$, *0.06 rad, 2nd cycle).*

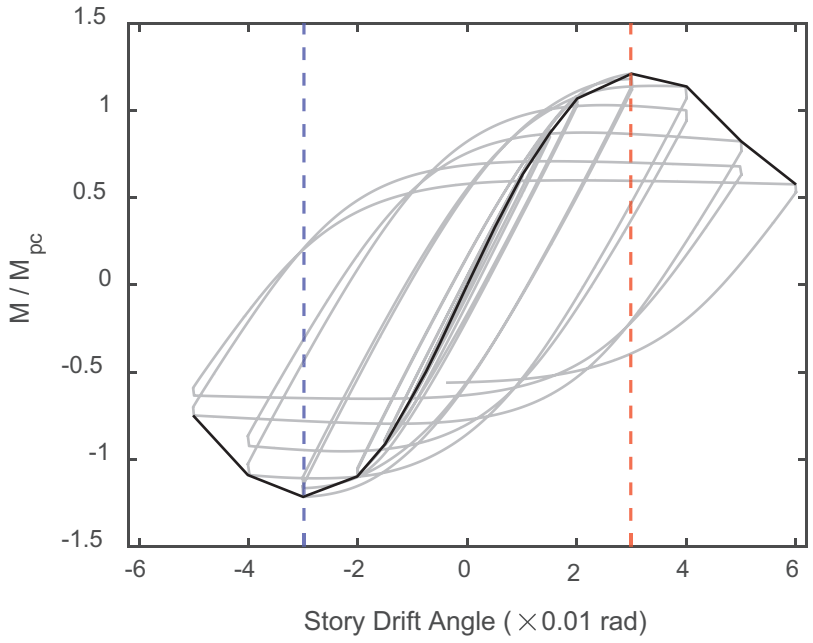

Fig. 3. Hysteretic response of nominal 6 × 6 × 0.25 in. specimen ($b/t = 23.9$, $L/r = 34.2$, *and* $P/P_{ya} = 0.15$*).*

(a) 3D view *(b) Global imperfection shape* *(c) Local imperfection shape*

Fig. 4. Finite element model of HSS columns.

work of Ozkula et al. (2021) to define adjusted critical story drift angles, or SDA'_{cr}.

Development of Seismic Local Buckling Limits

A few steps are needed for the transition from adjusted critical story-drift angle, or SDA'_{cr}, to seismic local buckling limits. First, the SDA'_{cr} values are set to performance targets for moderately and highly ductile members. SDA'_{cr} is defined as 0.02 rad for a moderately ductile column in an intermediate moment frame (IMF) and 0.04 rad for a highly ductile column in a special moment frame (SMF). Rewriting the SDA'_{cr} equations to define the b/t values provides equations for the moderately ductile, λ_{md}, and highly ductile, λ_{hd}, limits. Figure 6 compares proposed limits to those in the current AISC *Seismic Provisions* (2022b). The proposed highly and moderately ductile limits are in terms of C_a, a ratio between the factored axial load demand and the expected yield capacity of the column.

BUILT-UP BOX COLUMNS

The built-up box column research was another investigation that integrated experimental testing with computational simulations. The work was motivated by and extended previous research on the seismic behavior of built-up box columns. The beam-to-column subassemblage tests and finite element simulations further extended the work with characterization of boundary condition and near-fault loading effects for defining critical story-drift angles for the box columns. Revised seismic local buckling limits have been proposed based on this research.

Previous Testing on Built-Up Box Columns

Prior research on built-up box columns has informed current research efforts. Tests have been conducted on isolated columns, subassemblages, and full frames. The research has revealed some conservatism in the current seismic local buckling limits and provided direction for research underway.

Cyclic work of isolated columns has shown differences between wide-flange and built-up box columns, as well as potential improvements for box columns. Chou and Chen (2020) tested six large-scale, built-up box columns with fixed-fixed boundary conditions. Four columns were subjected to a constant axial load ($0.25–0.4P_y$) and cyclic lateral loading, and another two columns were subjected to a constant axial load ($0.4P_y$) and different near-fault lateral loadings. The columns performed well at high lateral drifts when the column satisfied the width-thickness limit for highly ductile members, λ_{hd} (AISC, 2022b). Lin and

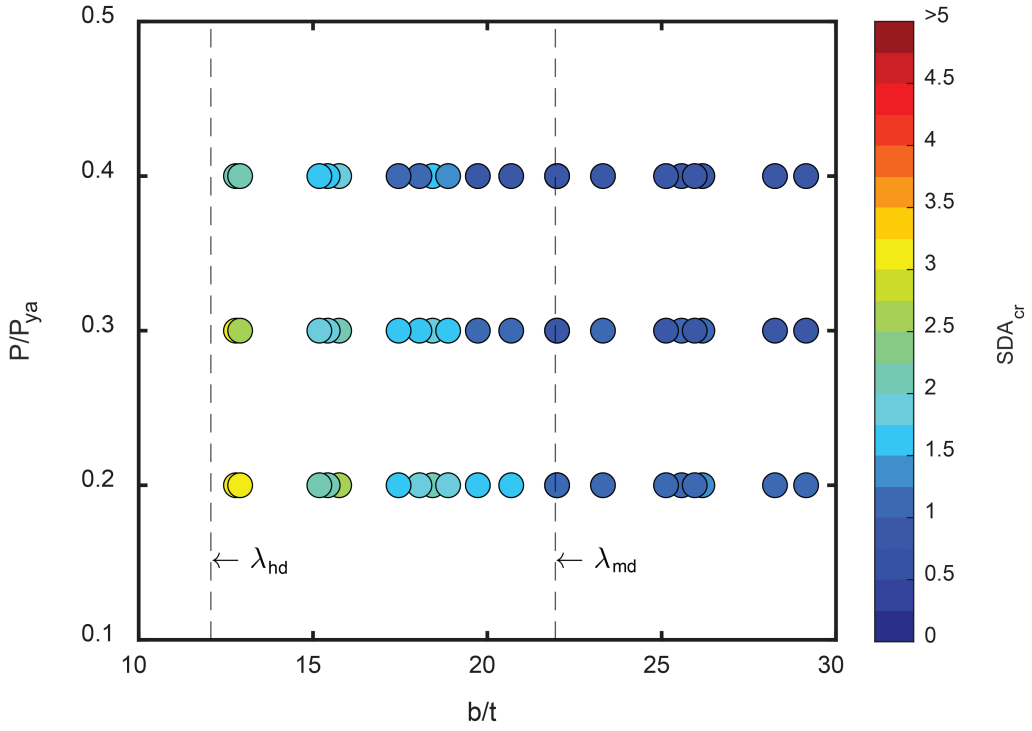

Fig. 5. Critical story drift angle (SDA_{cr}) of considered BCR295 sections.

Chou (2022) further tested deep wide-flange columns and built-up box columns, all satisfying the highly ductile member requirement, λ_{hd}. The work showed that (1) the AISC *Seismic Provisions* λ_{hd} limit results in markedly different cyclic responses for deep wide-flange columns and built-up box columns, and (2) the highly ductile member requirement, λ_{hd}, for built-up box columns is overly conservative.

The boundary conditions greatly influence column cyclic behavior. In multistory buildings, the connections and continuation to the beams and columns at the second story affect the lateral stiffness and deformation capacity of first-story columns. Chou et al. (2023) studied the first-story column behavior by adopting actual boundary conditions in steel multistory buildings. The first-story built-up box column tests were conducted by using a half-scale, beam-to-column subassemblage consisting of a two-and-a-half-story steel frame with I-shaped beams at two floors. Figure 7 shows the frame, a test specimen at 0.045 rad drift, and the column deformations at that level of drift. No yielding or buckling was observed at the top ends of the first-story columns. However, yielding at the bottom ends of the second-story columns was observed at medium lateral drifts for the highly ductile built-up box column because the strong column–weak beam (SCWB) requirement was met by a small margin based on the AISC *Seismic Provisions* (AISC, 2022b).

The boundary conditions and other parameters were studied in additional subassemblage tests. To further investigate the cyclic behavior of first-story built-up box columns under reversed cyclic lateral loading and constant axial loading, Chou et al. (2024a) conducted tests on subassemblage columns by using a full-scale, one-and-a-half-story subassemblage testing scheme (Figure 8). The columns had different width-thickness ratios (16.2 and 20.5) and axial load ratios ($0.25P_y$ and $0.4P_y$). Four subassemblages were designed with steel beams at the second floor and a moderately ductile built-up box column. All were able to achieve at least one complete test cycle at 0.04 rad drift without noticeable degradation in strength. Figure 8 shows a test specimen and the column local buckling at 0.05 rad lateral drift. By collecting moment and drift data at 0.02 and 0.04 rad from isolated column and subassemblage column tests, a relaxed b/t limit for the flange of highly ductile built-up box sections, $\lambda_{hd} = 0.96\sqrt{E/R_yF_{yn}}$, was proposed, significantly exceeding the current limit in (AISC, 2022b). Moreover, one additional subassemblage was tested using the hybrid simulation of a full-scale, seven-story steel dual frame, verifying the acceptable seismic performance of the moderately ductile built-up box column under varying axial compression load ($0.11–0.38P_y$) and lateral drifts to 1.5 times the maximum considered earthquake level (Wang et al., 2023).

Shake table tests complemented the experimental work on built-up box columns. Evaluating the seismic performance of moderately ductile built-up box columns in earthquakes, Chou et al. (2024b), conducted shake table tests on a full-scale, three-story steel dual frame (Figure 9) with a buckling-restrained braced frame and a special moment frame. The test results indicated that the b/t requirement for highly ductile built-up box columns in the AISC *Seismic Provisions* (2022b) is overly conservative. Columns with a large b/t value (e.g., 21), exceeding the highly ductile column requirement (λ_{hd} = 12.2), still provided satisfactory performance in the first story at large drifts without showing strength degradation (i.e., 0.038 rad).

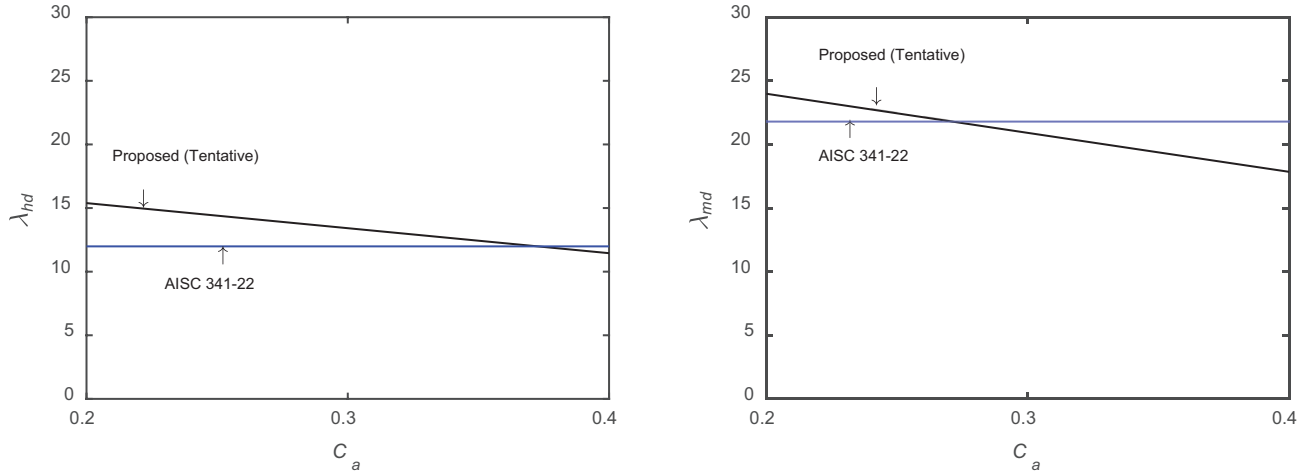

(a) Highly ductile *(b) Moderately ductile*

Fig. 6. Proposed highly and moderately ductile limits compared with current limits in the AISC Seismic Provisions.

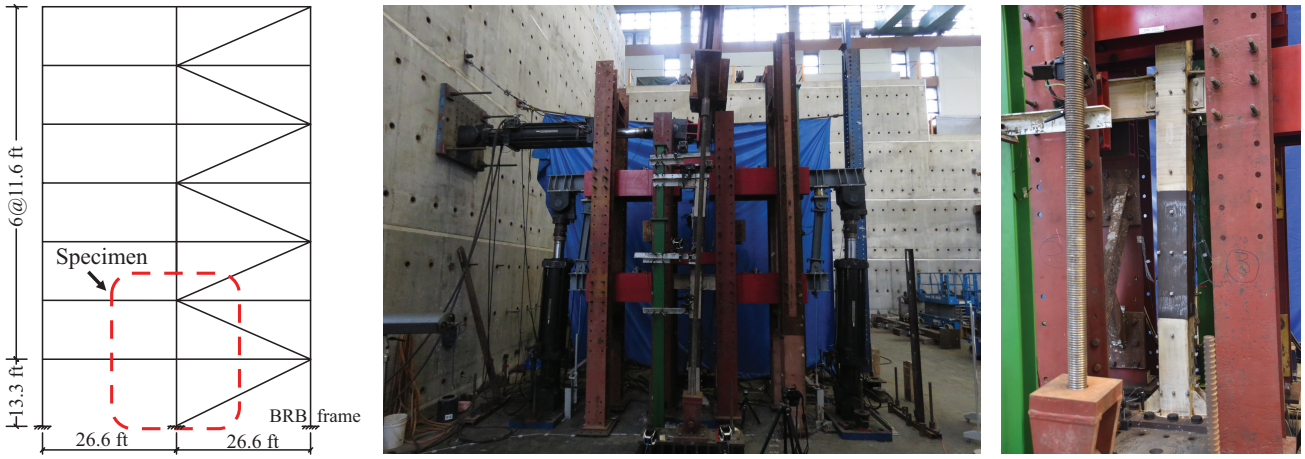

Fig. 7. Two-and-a-half-story steel beam-to-column subassemblage: (a) prototype frame, (b) deformation at 0.045 rad lateral drift, and (c) column deformation after 0.045 rad lateral drift.

Fig. 8. One-and-a-half story steel beam-to-column subassemblage: (a) deformation at 0.05 rad lateral drift and (b) column local buckling after 0.05 rad lateral drift.

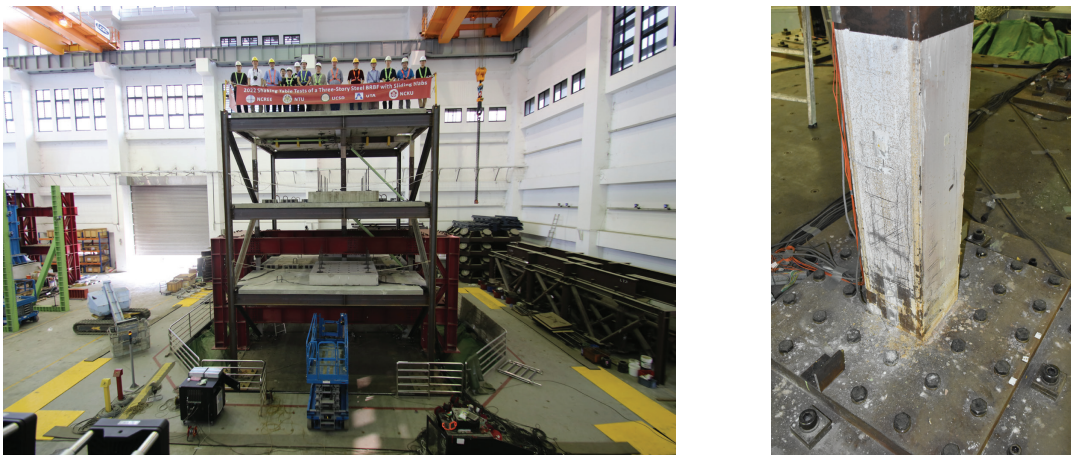

Fig. 9. Shake table testing of a steel (a) three-story dual system and (b) a column base after testing (2.7MCE level).

Test Specimens, Setup, and Loading Protocol

The research team has conducted cyclic lateral tests on 10 square built-up box columns with varying element slenderness and axial loading. Four of the tests were from the previous study by Chou and Chen (2020). The walls of the box columns were joined by complete-joint-penetration (CJP) groove welds as shown in Figure 10. The SN 490B steel had a specified minimum yield stress of 47.1 ksi. Outside dimensions for the specimens ranged from 12 to 16 in., and thicknesses ranged from 0.5 to 1.125 in. The resulting width-thickness (b/t) ratios were from 11.8 to 36. Ratios lower than 15.4 satisfy λ_{hd}, the width-to-thickness limit for a highly ductile member, while ratios lower than 23.7 satisfy λ_{hd}, the limit for a moderately ductile member (AISC, 2022b). The 2020 specimens included two highly ductile and two moderately ductile columns. The remaining specimens, tested in 2024, all exceeded the moderately ductile member limit. The specimens were subjected to axial compression and cyclic lateral loading. The Multi-Axial Testing System (MATS) (Figure 1) was used to impose the loading and fixed-fixed boundary conditions. These columns were subjected to a constant axial load of 0.2 to 0.4 times the axial yield capacity. Cycles of increasing lateral drift were applied following the standard loading protocol of the AISC *Seismic Provisions* (AISC, 2022b) for testing special moment connections.

Experimental Results

As with the HSS columns, the built-up box columns exhibited overall similar behavior with differences in the hysteretic response. Local buckling was observed at the ends of the columns. Flange fracture close to the CJP weld also occurred in the 2024 box columns. Axial load effects can be seen in the moment versus rotation results. Figure 11 shows moment-rotation plots for columns with the same b/t but twice the axial load for one of the specimens. The higher axial load results in a lower peak moment and deformation capacity. Trends with b/t values were also observed.

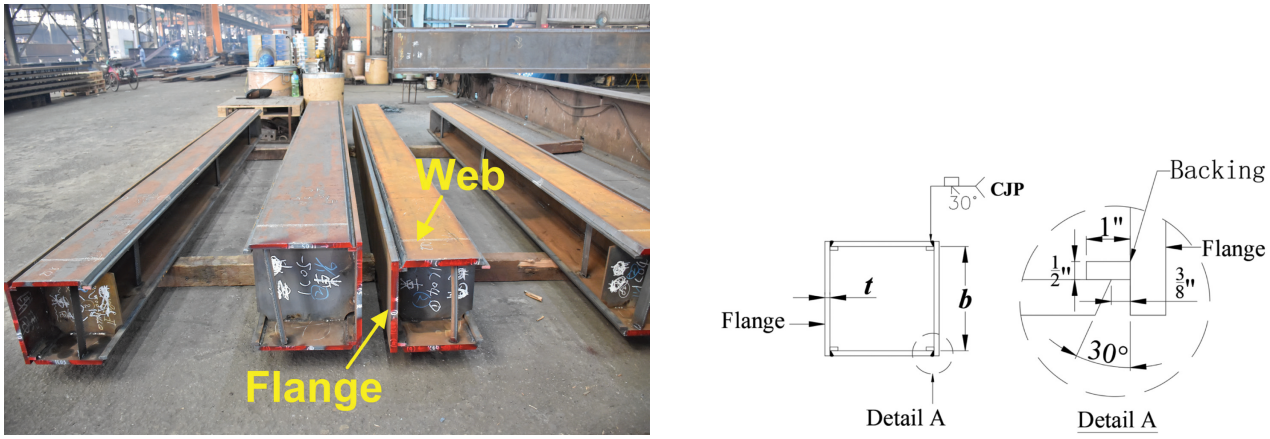

(a) In fabrication *(b) Complete-joint-penetration (CJP) groove welds*

Fig. 10. Built-up box column assembly.

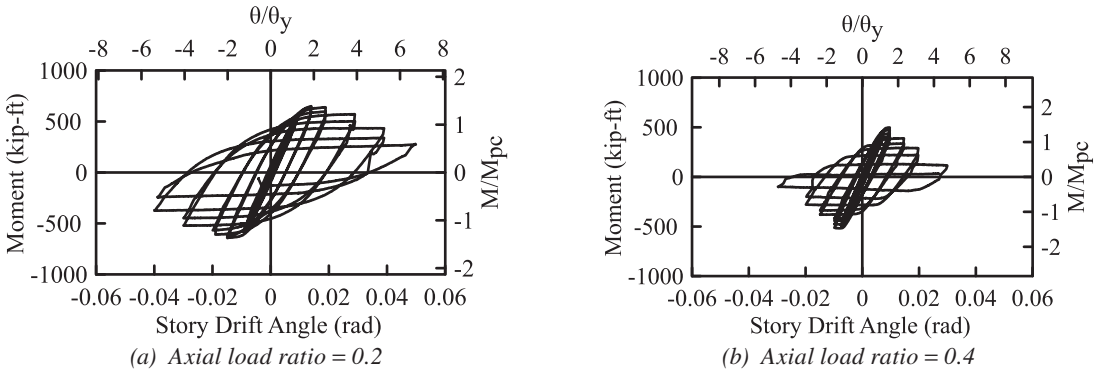

(a) Axial load ratio = 0.2 *(b) Axial load ratio = 0.4*

Fig. 11. Moment-rotation responses for built-up columns with b/t = *36.*

The first four columns (Chou and Chen, 2020) performed well with SDA_{cr} values of 0.03 and 0.04, the latter for those satisfying the highly ductile member requirement λ_{hd} in the AISC *Seismic Provisions* (AISC, 2022b). The next six columns, which exceeded the moderately ductile limit, exhibited lower ductility (e.g., SDA_{cr} values from 0.01 to 0.02) and strength degradation.

Finite Element Simulations

Subassemblage test results were used to characterize a boundary condition factor on the isolated columns. Finite element analysis program ABAQUS (2016) was used to characterize loading effects (cyclic versus near-fault loadings) on the isolated columns. The team developed models of the test specimens, subjected them to the same loading protocols, and compared the experimental to the computational results (Figure 12). The observed local buckling and moment-rotation results compared well between the physical experiments and the computational simulations. Finite element comparisons were also made between the fixed-fixed isolated columns under the standard cyclic loading of the AISC *Seismic Provisions* and the near-fault loading from Lin and Chou (2022) to develop a loading factor. The two factors were used to define the adjusted critical story-drift angle, or SDA'_{cr}, with modifications of the isolated column test results for boundary conditions and loading protocol effects (Ozkula et al., 2021).

Development of Seismic Local Buckling Limits

The research results have been used to develop proposals for seismic local buckling limits for square, built-up box columns. Following the methodology for I-shaped deep

(a) Local buckling in the experiment

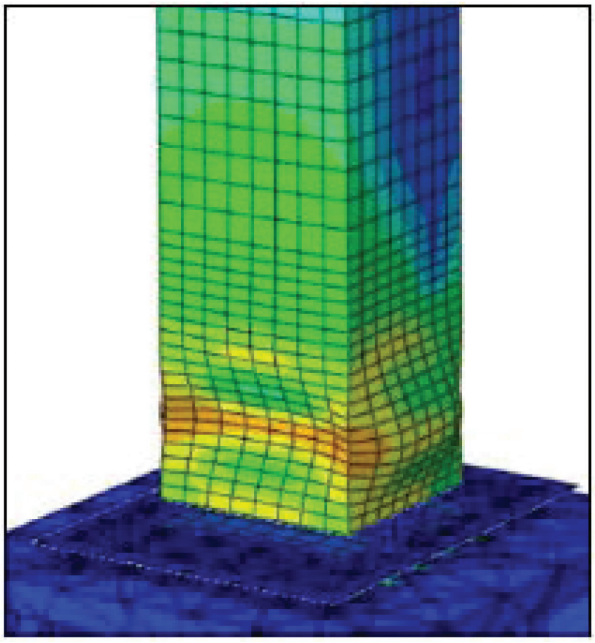

(b) Local buckling observed in FEA

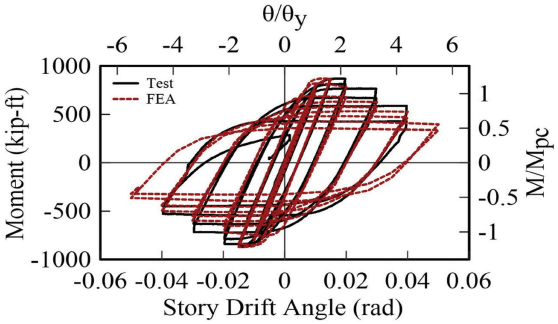

(c) Comparison of the experimental versus finite element analysis moment-rotation results

Fig. 12. Sample isolated column.

columns (Ozkula et al., 2021), the team proposed preliminary revised seismic b/t limits that are dependent on the column axial load ratio (Figure 13). Figure 13 shows the proposed highly and moderately ductile limits in terms of C_a, a ratio between the factored axial load demand and the expected yield capacity of the column. Comparisons to the current AISC limits (AISC, 2022b) are also shown. The experimental results had indicated that the current highly ductile and moderately ductile b/t limits for square built-up box members in the AISC *Seismic Provisions* are too conservative except for the columns under a very high constant axial load (0.4–0.5 times the axial yield capacity). The proposed limits capture the axial load effect and remove the conservatism for lower axial loads.

FUTURE WORK

The featured work has focused on the seismic performance of square HSS and built-up box columns. Cyclic testing included isolated HSS and box columns, as well as subassemblage and shake table testing for the built-up box columns. Previous work had found some member width-to-thickness limits to be too conservative. The investigations presented here resulted in preliminary proposals for revised seismic b/t limits. Future research needs include investigation into the observed fracture of CJP groove welds caused by severe buckling in the built-up box columns. Future work may also include tests with bi-directional lateral loading together with axial load on the column. The researchers would like to extend the half-scale HSS work with full-scale experiments to further verify the simulation results and the proposed equations. Differences across steel grades (e.g., A500, A1085, STKR, BCR) may also be studied. Meanwhile, future work plans include similar studies of non-square HSS and built-up box column members with different width-to-thickness ratios for webs and flanges.

ACKNOWLEDGMENTS

Thank you to Dr. Chou and Dr. Wu for all the materials, coordination, edits, and other feedback and contributions. The contributions of Nicholas Tedjasukmana, Guan-Wei Chen, Hou-kan Sen, Chien-Ting Weng, and Yu-Wen Teng of NTU and Chi-Rung Jian (NCREE) are also acknowledged. The research is sponsored by the National Science and Technology Council, Taiwan. The researchers would also like to thank collaborators Dr. Jason McCormick (University of Michigan) and Dr. Chia-Ming Uang (University of California–San Diego). Any findings or recommendations are those of the researchers and do not necessarily reflect the views of the sponsors.

REFERENCES

ABAQUS (2016), *ABAQUS/CAE User's Guide 6.13*, Dassault Systemes Simulia Corporation, Waltham, Mass.

AISC (2022a), *Specification for Structural Steel Buildings*, ANSI/AISC 360-22, American Institute of Steel Construction, Chicago, Ill.

AISC (2022b), *Seismic Provisions for Structural Steel Buildings*, ANSI/AISC 341-22, American Institute of Steel Construction, Chicago, Ill.

Chou, C.-C. and Chen, G.-W. (2020), "Lateral Cyclic Testing and Backbone Curve Development of High-Strength Steel Built-Up Box Columns under Axial Compression," *Engineering Structures*, Vol. 223, 111147.

Chou, C.-C., Lin, H.-Z., Córdova, A., Chen, J.-M., Chou, Y.-H.D., Chao, S.-H. Chao, S.-H., Tsampras, G., Uang, C.-M., Chung, H.-Y., Loh, C.-H., and Hu, H.-T. (2024b), "Earthquake Simulator Testing of a Three-Story Steel Building for Evaluating Built-Up Box Column Performance and Effect of Sliding Slab," *Earthquake Engineering and Structural Dynamics*, https://doi.org/10.1002/eqe.4130.

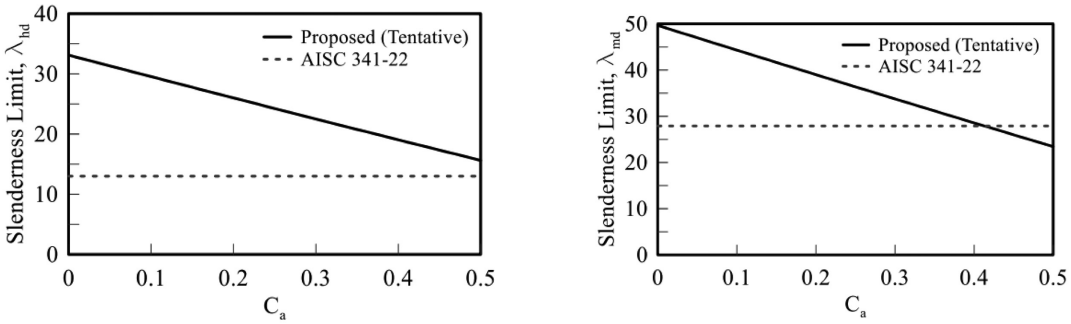

(a) Highly ductile *(b) Moderately ductile*

Fig. 13. Preliminary revised seismic b/t *limits.*

Chou, C.-C., Shen, H.-K., and Chou, Y.-H.D. (2024a), "Subassemblage Test and Width-Thickness Design Limit for Steel Built-Up Box Columns Subjected to Axial Load and Cyclic Lateral Drift," *Engineering Structures*, Vol. 308, 118023.

Chou, C.-C., Xiong, H.-C., Kumar, A., Lai, Y.C., and Uang, C.M. (2023), "Effects of Section Compactness and SCWB Condition on Moment Redistribution and Plastic Hinging in SMF Built-up Box Columns," *Journal of Structural Engineering,* ASCE, Vol. 149, No. 11, 04023144.

Lin, T.-H. and Chou, C.-C. (2022), "High-Strength Steel Deep H-Shaped and Box Columns under Proposed Near-Fault and Post-Earthquake Loadings," *Thin-Walled Structures*, Vol. 172, 108892.

LS DYNA (2013), *LS-DYNA Keyword User's Manual*, Livermore Software Technology, Livermore, Calif.

Ozkula G., Uang C.-M., and Harris J. (2021), "Development of Enhanced Seismic Compactness Requirements for Webs in Wide-Flange Steel Columns," *Journal of Structural Engineering*, ASCE, Vol. 147, No. 7.

Takeshi, I. and Takuya, M. (2020, March), "Overview of Construction Products and Methods in JFE Group," JFE Technical Report, No. 25, JFE Steel Corporation.

Teng, Y.-W., Wu, T.-Y., Weng, C.-T., and Jiang, C.-R. (2023), "Seismic Performance of Square HSS Columns," *34th KKHTCNN Symposium on Civil Engineering*, Pattaya, Thailand. (abstract only).

Wang, K.-J., Chou, C.-C., Huang, C.-W., Shen, H.-K., Sepulveda, C., Mosqueda, G., and Uang, C.-M. (2023), "Hybrid Simulation of a Steel Dual System with Buckling-Induced First-Story Column Shortening: A Mixed Control Mode Approach," *Earthquake Engineering and Structural Dynamics*, Vol. 52, No. 12, pp. 3,727–3,745. DOI: 10.1002/eqe.3944.

Guide for Authors

Scope

Engineering Journal is dedicated to the improvement and advancement of steel construction. Its pages are open to all who wish to report on new developments or techniques in steel design, research, the design and/or construction of new projects, steel fabrication methods, or new products of significance to the uses of steel in construction. Only original papers should be submitted.

General

Papers intended for publication should be submitted by email Margaret Matthew, editor, at **matthew@aisc.org**.

The articles published in the *Engineering Journal* undergo peer review before publication for (1) originality of contribution; (2) technical value to the steel construction community; (3) proper credit to others working in the same area; (4) prior publication of the material; and (5) justification of the conclusion based on the report.

All papers within the scope outlined above will be reviewed by engineers selected from among AISC, industry, design firms, and universities. The standard review process includes outside review by an average of three reviewers, who are experts in their respective technical area, and volunteers in the program. Papers not accepted will not be returned to the author. Published papers become the property of the American Institute of Steel Construction and are protected by appropriate copyrights. No proofs will be sent to authors.

Manuscripts

Manuscripts must be provided in Microsoft Word format. Include a PDF with your submittal so we may verify fonts, equations and figures. View our complete author guidelines at **aisc.org/ej**.

Smarter. Stronger. Steel.

American Institute of Steel Construction
130 E Randolph St, Ste 2000, Chicago, IL 60601
312.670.2400 | aisc.org/ej